

# Stellar Ly $\alpha$ Emission Lines in the *Hubble Space Telescope* Archive: Intrinsic Line Fluxes and Absorption from the Heliosphere and Astrospheres<sup>1</sup>

Brian E. Wood<sup>2</sup>, Seth Redfield<sup>3</sup>, Jeffrey L. Linsky<sup>2</sup>, Hans-Reinhard Müller<sup>4,5</sup>, Gary P. Zank<sup>5</sup>

## ABSTRACT

We search the *Hubble Space Telescope* (HST) archive for previously unanalyzed observations of stellar H I Ly $\alpha$  emission lines, our primary purpose being to look for new detections of Ly $\alpha$  absorption from the outer heliosphere, and to also search for analogous absorption from the astrospheres surrounding the observed stars. The astrospheric absorption is of particular interest because it can be used to study solar-like stellar winds that are otherwise undetectable. We find and analyze 33 HST Ly $\alpha$  spectra in the archive. All the spectra were taken with the E140M grating of the Space Telescope Imaging Spectrograph (STIS) instrument on board HST. The HST/STIS spectra yield 4 new detections of heliospheric absorption (70 Oph,  $\xi$  Boo, 61 Vir, and HD 165185) and 7 new detections of astrospheric absorption (EV Lac, 70 Oph,  $\xi$  Boo, 61 Vir,  $\delta$  Eri, HD 128987, and DK UMa), doubling the previous number of heliospheric and astrospheric detections. When combined with previous results, 10 of 17 lines of sight within 10 pc yield detections of astrospheric absorption. This high detection fraction implies that most of the ISM within 10 pc must be at least partially neutral, since the presence of H I within the ISM surrounding the observed star is necessary for an astrospheric detection. In contrast, the detection percentage is only 9.7% (3 out of 31) for stars beyond 10 pc. Our Ly $\alpha$  analyses provide measurements of ISM H I and D I column densities for all 33 lines of sight, and we discuss some implications of these results. Finally, we measure chromospheric Ly $\alpha$  fluxes from the observed stars. We use these fluxes to determine how Ly $\alpha$  flux correlates with coronal X-ray and chromospheric Mg II emission, and we also study how Ly $\alpha$  emission depends on stellar rotation.

---

<sup>1</sup>Based on observations with the NASA/ESA Hubble Space Telescope, obtained at the Space Telescope Science Institute, which is operated by the Association of Universities for Research in Astronomy, Inc., under NASA contract NAS5-26555.

<sup>2</sup>JILA, University of Colorado and NIST, Boulder, CO 80309-0440; woodb@origins.colorado.edu, jlin-sky@jila.colorado.edu.

<sup>3</sup>Harlan J. Smith Postdoctoral Fellow, McDonald Observatory, University of Texas, Austin, TX 78712-0259; sredfield@astro.as.utexas.edu.

<sup>4</sup>Department of Physics and Astronomy, Dartmouth College, 6127 Wilder Lab, Hanover, NH 03755-3528; Hans.Mueller@Dartmouth.edu.

<sup>5</sup>Institute of Geophysics and Planetary Physics, University of California at Riverside, 1432 Geology, Riverside, CA 92521; zank@ucr.ac1.ucr.edu.

*Subject headings:* circumstellar matter — ISM: structure — stars: chromospheres — stars: winds, outflows — ultraviolet: ISM — ultraviolet: stars

## 1. INTRODUCTION

High resolution spectra of H I Ly $\alpha$  lines from the *Hubble Space Telescope* (HST) have proven to be useful for many purposes. Hydrogen and deuterium atoms in the interstellar medium produce absorption features in stellar Ly $\alpha$  spectra that can be analyzed to yield information about the ISM. Of particular interest are measurements of the local deuterium-to-hydrogen (D/H) ratio, which has been a focal point for these analyses in the past due to its relevance for cosmology and Galactic chemical evolution (e.g., Linsky et al. 1995a; Dring et al. 1997; Linsky 1998; Vidal-Madjar et al. 1998; Wood et al. 2004).

In addition to the ISM absorption, some of the Ly $\alpha$  spectra of nearby stars also show absorption from the outer heliosphere and/or absorption from the analogous “astrospheres” surrounding the observed stars (Linsky & Wood 1996; Wood, Alexander, & Linsky 1996a; Gayley et al. 1997). The region of the outer heliosphere that is probed by the heliospheric absorption is not observable by any other means. Astrospheres and the solar-like stellar winds that are implied by their presence are also otherwise completely undetectable. Thus, the heliospheric and astrospheric diagnostics provided by the HST Ly $\alpha$  absorption spectra are truly unique. Wood (2004) provides a complete review of past results concerning the analysis of the heliospheric and astrospheric absorption.

The most important quantitative results from the astrospheric Ly $\alpha$  absorption analyses are the first measurements of mass loss rates for solar-like stars, although they could also in principle be used as ISM diagnostics (Frisch 1993). Collectively, these measurements suggest that mass loss increases with magnetic activity and decreases with stellar age, suggesting that the solar wind was stronger in the past (Wood et al. 2002b). In addition to its obvious importance for solar/stellar astronomy, the implied stronger wind of the young Sun could have important ramifications for our understanding of the evolution of planetary atmospheres in our solar system. However, the inferred mass-loss/activity and mass-loss/age relations for cool main sequence stars are based on only six astrospheric detections. Many more detections are necessary to confirm and refine these results.

Motivated primarily by the need to increase the number of astrospheric detections, we have searched the HST archive for additional Ly $\alpha$  spectra of nearby cool stars. We find 33 new data sets to analyze. In addition to identifying lines of sight with detectable astrospheric absorption, we also analyze these data for other purposes: (1) To search for heliospheric Ly $\alpha$  absorption, (2) To measure ISM H I column densities, and (3) To measure chromospheric Ly $\alpha$  fluxes corrected for ISM, heliospheric, and astrospheric absorption. By combining our results with previous measurements, we ultimately provide here a complete list of Ly $\alpha$  measurements based on high resolution HST

spectra of nearby cool stars, and we discuss some implications of these results.

## 2. THE DATABASE OF HST Ly $\alpha$ SPECTRA

In the top section of Table 1, we list 29 lines of sight with HST Ly $\alpha$  spectra that have been analyzed and published. (See the references listed in the last column of the table.) Except for 36 Oph A, all these spectra were taken by the Goddard High Resolution Spectrograph (GHRS) instrument. The 36 Oph A spectrum was taken by the Space Telescope Imaging Spectrograph (STIS), which replaced the GHRS on HST in 1997.

The eighth column of Table 1 lists the ISM H I column densities (in  $\text{cm}^{-2}$ ) measured towards the observed stars. The ninth column indicates whether high resolution HST spectra of the interstellar Mg II h & k absorption lines (at 2803 Å and 2796 Å, respectively) are available to provide information on the velocity structure of the ISM. When available, this information is always taken into account in the analysis of the broad, saturated ISM Ly $\alpha$  absorption, which increases confidence in the results of the complex Ly $\alpha$  analysis. Note that only the highest resolution gratings of the GHRS and STIS instruments, with  $R \equiv \lambda/\Delta\lambda \approx 100,000$ , can resolve the narrow Mg II absorption lines, so column 8 of Table 1 does not acknowledge the presence of low ( $R \approx 1000$ ) or moderate ( $R \approx 25,000$ ) resolution spectra of Mg II in the HST archive.

The tenth and eleventh columns of Table 1 indicate which Ly $\alpha$  spectra show the presence of heliospheric absorption and astrospheric absorption, in addition to the ISM absorption. Marginal detections are indicated by question marks. Whether a detection is marginal or not is based on our own determination, after inspecting and working with the data ourselves. Lemoine et al. (2002) and Vidal-Madjar & Ferlet (2002) find evidence for weak heliospheric absorption towards the similar Capella and G191-B2B lines of sight, but these claims rely on subtle statistical arguments rather than clearly visible excess absorption, so we do not consider these to be detections for our purposes here.

For eight of the stars in Table 1, the tenth and eleventh columns are left blank because the Ly $\alpha$  spectra are moderate resolution GHRS spectra, which generally lack sufficient spectral resolution to allow a clear detection of heliospheric or astrospheric absorption. The exception is Sirius, which shows detectable heliospheric absorption in its moderate resolution GHRS spectrum (Izmodenov, Lallement, & Malama 1999b). This detection owes its success in large part to the extremely low ISM H I column density for that line of sight, which minimizes the ISM absorption and makes the heliospheric absorption easier to detect. Nearly all of the stars listed in Table 1 are cool stars, but there are a few exceptions: Sirius, HZ 43, G191-B2B, Feige 24, and GD 246. These stars will not have solar-like astrospheres around them since they do not have solar-like winds. For this reason, column 11 is left blank for these stars.

Our goal here is to find additional Ly $\alpha$  spectra lurking in the HST archive to provide new measurements of ISM absorption, and hopefully new detections of heliospheric and astrospheric

absorption. We confine our attention to lines of sight shorter than 100 pc. Longer lines of sight will almost certainly have ISM H I column densities too high and ISM Ly $\alpha$  absorption too broad to hope to detect any heliospheric or astrospheric absorption. We also restrict ourselves to observations of cool stars of spectral type F and later, which will presumably have coronal winds analogous to that of the Sun and will therefore potentially have detectable astrospheres analogous to the Sun’s heliosphere.

Finally, the Ly $\alpha$  spectra must have sufficient spectral resolution to allow for a reasonably confident identification of heliospheric and astrospheric absorption, if present. Ideally, this means high resolution spectra with either the GHRS Ech-A grating or the STIS E140H grating, which are both capable of fully resolving the H I and D I Ly $\alpha$  absorption line profiles. Unfortunately, all the Ech-A and E140H data that fit our criteria have already been analyzed and are listed in the top section of Table 1. As mentioned above, the  $R \approx 25,000$  moderate resolution GHRS spectra do not generally have sufficient spectral resolution for our purposes. In order to clearly identify the presence of heliospheric and astrospheric absorption, which is always highly blended with the ISM absorption, it is necessary to use the information provided by the ISM D I absorption profile to constrain the ISM H I absorption, so resolving D I is crucial (see §4.2).

Although moderate resolution GHRS spectra do not meet our resolution requirements, moderate resolution STIS spectra with the E140M grating *are* acceptable. The STIS E140M spectra have  $R \approx 45,000$ , which is sufficient to mostly resolve the D I absorption profile. Furthermore, STIS E140M spectra cover a wide wavelength range of 1150–1730 Å, meaning that there are many E140M spectra in the HST archive taken to observe different emission lines within E140M’s broad spectral range that will nevertheless also include the Ly $\alpha$  line at 1216 Å in which we are interested.

We have searched the HST archive for previously unanalyzed STIS E140M spectra of cool stars within 100 pc, and in the bottom portion of Table 1 we list the 33 lines of sight observed by HST that meet these criteria. All observations except those of  $\xi$  Boo A and 61 Vir were performed through the  $0.2'' \times 0.2''$  aperture. The  $\xi$  Boo A and 61 Vir data were obtained through the narrower  $0.2'' \times 0.06''$  aperture. The data were reduced using the STIS team’s CALSTIS software package written in IDL (Lindler 1999). The processing includes wavelength calibration using spectra of the calibration lamp taken during the observations, and includes correction for scattered light. We generally coadd all available E140M spectra in the archive, with two exceptions. For AD Leo, there are separate data sets on 2000 March 10 and 2002 June 1. We choose not to include the latter because the geocoronal Ly $\alpha$  emission is difficult to remove in those data. (See §3 for more discussion about the geocoronal emission and its removal.) For V471 Tau, there are three different large data sets. For the sake of simplicity, we choose to reduce only the observations taken on 2000 August 24–27.

### 3. THE GEOCORONAL Ly $\alpha$ EMISSION

Figure 1 shows the final processed spectra of all 33 stars, focusing on the Ly $\alpha$  region. Each spectrum shows a stellar emission line upon which is superimposed a very broad H I Ly $\alpha$  absorption feature centered near the rest wavelength of 1215.670 Å. The spectra also show narrow D I Ly $\alpha$  absorption about  $-0.33$  Å from the center of the H I absorption, except in cases where the H I absorption is broad enough to obscure the D I absorption (see §4.2).

Finally, the spectra are contaminated by H I Ly $\alpha$  emission from the Earth’s geocorona, which is shaded in Figure 1. These geocoronal lines are narrow, and most are conveniently contained within the saturated core of the ISM H I absorption, allowing them to be easily removed. In such cases, we remove the geocoronal lines by fitting Gaussians to the lines and then subtracting the Gaussians from the data. Note that the HD 209458 spectrum is the sum of spectra taken at two different times when the geocoronal emission was at different wavelengths, so two Gaussians are fitted to the data in this case.

In some cases the geocoronal emission is blended with the sides of the H I absorption profile, making the geocoronal subtraction significantly harder and more uncertain (e.g., HD 73350). In such instances, we still use Gaussian fitting to estimate the absorption, but we only fit the side of the emission close to the absorption core and we force the fitted Gaussian to be at the expected wavelength, which we know to within about  $2 \text{ km s}^{-1}$  based on the accuracy of the wavelength calibration (see below). Nevertheless, the uncertainty in the geocoronal subtraction for these blended cases could be a significant source of systematic error in the analysis of the H I absorption lines. In all future figures, Ly $\alpha$  spectra will be shown with the geocoronal emission removed.

Although the geocoronal emission is an annoyance when it is blended with the sides of the absorption profile, its presence is actually beneficial when it is fully within the absorption core, because it can be used as a secondary wavelength calibrator. The data reduction places the spectra in a heliocentric rest frame, which means that the geocoronal emission is centered at the projected velocity of the Earth towards the star at the time of observation. This quantity is known accurately and can be compared with the measured center of the emission, in order to test the wavelength scale. In Figure 2, we plot the velocity discrepancies of the geocoronal emission from their expected locations ( $\Delta v \equiv v_{\text{obs}} - v_{\text{geo}}$ ) for all the newly analyzed stars. These are all STIS E140M spectra, so this represents an excellent test of the STIS E140M wavelength calibration.

The weighted mean and standard deviation of the data points in Figure 2 is  $\Delta v = -1.20 \pm 0.90 \text{ km s}^{-1}$ . This result suggests that CALSTIS-processed E140M spectra are systematically blueshifted by  $1.2 \text{ km s}^{-1}$  from where they should be, at least in the Ly $\alpha$  spectral region. The standard CALSTIS data reduction computes a global wavelength offset for the entire STIS spectrum from the wavelength calibration images. Perhaps the Ly $\alpha$  spectral region, which is near the edge of the E140M grating’s spectral coverage, is systematically shifted from the average offset value. There are also a few individual spectra that show significant discrepancies of up to  $4 \text{ km s}^{-1}$  from the average  $\Delta v$  value. Whatever the cause of the systematic wavelength shift and the scatter around

it, we believe that the geocoronal lines provide a better velocity scale, so for all spectra in which a geocoronal emission centroid can be measured, we correct the wavelengths of our spectra using the  $\Delta v$  values in Figure 2.

## 4. ANALYZING THE Ly $\alpha$ ABSORPTION LINES

### 4.1. Reconstructing the Stellar H I Ly $\alpha$ Profile

The D I Ly $\alpha$  absorption lines are relatively easy to analyze by themselves. Because they are narrow, a reasonably accurate continuum can be interpolated over these lines and an absorption profile can then be fitted to the D I lines. Redfield & Linsky (2004a) have already performed these measurements for some of the stars in our sample. Figure 3 shows examples of some of the D I fits. The thin solid line shows the assumed background continuum, the dotted lines show the individual absorption components of the fit, and the thick solid line shows the combination of all the components after convolution with the instrumental line spread function (LSF). The STIS E140M LSF used here is from Sahu et al. (1999).

Analyzing the H I Ly $\alpha$  absorption is much trickier. Not only is the visible absorption broad and difficult to interpolate over, but ISM H I column densities towards even the nearest stars are high enough for the H I absorption profile to have extended damping wings. Thus, analyzing the H I absorption essentially requires first reconstructing the entire stellar Ly $\alpha$  profile. This can be done as follows.

The first step is to use a fit to the D I absorption to infer what the central wavelength and Doppler broadening parameter should be for the H I line. The ISM H I absorption should presumably have the same centroid velocity as D I, so  $v(\text{H I}) = v(\text{D I})$ , and since past work has demonstrated that H I and D I absorption lines in the local ISM are dominated by thermal broadening (e.g., Linsky & Wood 1996; Redfield & Linsky 2004b), their Doppler parameters are related by  $b(\text{H I}) \approx \sqrt{2}b(\text{D I})$ . With this information, an H I opacity profile,  $\tau_\lambda$  (assumed to be a Voigt profile), can be computed for various assumed values of the H I column density,  $N(\text{H I})$ . For each opacity profile, we can then reconstruct the wings of the stellar emission line profile by multiplying the data by  $\exp(\tau_\lambda)$ . (Note that since we are interested in modeling the damping wings rather than the central part of the absorption, the assumed value of  $b(\text{H I})$  is actually unimportant.)

Figure 4 shows the results of this exercise using the  $\xi$  Boo data as an example, with the D I absorption having been removed. Stellar line profiles are reconstructed assuming ISM H I column densities in the range  $\log N(\text{H I}) = 17.6 - 18.2$  (units  $\text{cm}^{-2}$ ). Only the wings of the profile outside the dashed lines are reconstructed using the opacity profiles computed as described above. In order to estimate the profile in between the dashed lines, we either use a polynomial fit to the wings to interpolate between them, or more commonly we use the Mg II h & k lines to estimate the shape of the central portion of the Ly $\alpha$  profile. The justification for this is that Ly $\alpha$  and the two Mg II lines

are all highly optically thick chromospheric lines that have similar profiles in the solar spectrum (Donnelly, White, & Livingston 1994; Lemaire et al. 1998). Table 1 indicates which HST data sets include high resolution Mg II spectra. If high resolution Mg II spectra are not available for a star, we often use the Mg II profile of a similar star. (The  $\xi$  Boo A Mg II profiles are the most commonly used surrogates.)

#### 4.2. Fitting the ISM Absorption

The profile reconstruction technique described in §4.1 results in a family of stellar Ly $\alpha$  profiles, as in Figure 4, each of which can be used as a starting point for an analysis of the H I absorption. With each assumed profile, an initial H I+D I absorption fit is performed, which is done using a  $\chi^2$  minimization technique (Bevington & Robinson 1992). All necessary atomic data for the D I and H I Ly $\alpha$  lines are taken from Morton (2003). The absorption is convolved with the LSF before comparing with the data, as in the D I fits in Figure 3. In all our fits involving H I absorption, we fit H I and D I simultaneously and constrain the problem by forcing  $v(\text{H I}) = v(\text{D I})$  and  $b(\text{H I}) = \sqrt{2}b(\text{D I})$ . After the initial fit, the assumed stellar profile is then altered based on the residuals of the fit, and then a second, presumably improved absorption line fit is performed. Additional iterations can be done to further refine the fit. For a simple line of sight with one ISM absorption component and no heliospheric or astrospheric absorption, the problem is well constrained enough that this iterative process ultimately ends up driving the fit parameters of the single absorption component towards the same solution *no matter which of the assumed stellar profiles one actually starts out with*. However, this is not always the case in more complicated multi-component lines of sight, especially when heliospheric or astrospheric absorption is present (see Linsky & Wood 1996).

Fortunately, it is possible to constrain the analysis even further by assuming a D/H ratio. Using UV spectra from HST and the *Far Ultraviolet Spectroscopic Explorer* (FUSE), a consensus has been reached that the interstellar D/H ratio is invariable within the Local Bubble. Based on different compilations of measurements, Linsky (1998) finds  $\text{D}/\text{H} = (1.50 \pm 0.10) \times 10^{-5}$ , Moos et al. (2002) quotes  $\text{D}/\text{H} = (1.52 \pm 0.08) \times 10^{-5}$ , and Wood et al. (2004) computes  $\text{D}/\text{H} = (1.56 \pm 0.04) \times 10^{-5}$ , with no evidence for significant variation within 100 pc.

Since all our targets are located within the Local Bubble, we simply assume  $\text{D}/\text{H} = 1.5 \times 10^{-5}$ , consistent with the values quoted above. With the addition of this assumption, all three fit parameters of the difficult-to-analyze H I absorption [ $v(\text{H I})$ ,  $b(\text{H I})$ , and  $N(\text{H I})$ ] are dependent on the much better constrained D I fit parameters [ $v(\text{D I})$ ,  $b(\text{D I})$ , and  $N(\text{D I})$ ]. The ISM H I absorption profile is therefore much more tightly constrained, even when multiple ISM components are included. This assumption also means that we do not have to experiment with all the stellar profiles reconstructed as in Figure 4. We can instead immediately focus on the profile that was constructed assuming the  $N(\text{H I})$  value that the D I fit suggests should yield  $\text{D}/\text{H} = 1.5 \times 10^{-5}$ . In the case of  $\xi$  Boo A that value is  $\log N(\text{H I}) = 17.9$ , and this profile is emphasized in Figure 4.

Not having to consider the other profiles as possible starting points for the H I absorption analysis greatly simplifies what would otherwise be a formidable and time-consuming problem considering the number of spectra that we wish to analyze.

In order to provide the reader with an idea of how H I+D I absorption profiles vary under the constraints described above, Figure 5 shows profiles computed for a range of column densities,  $\log N(\text{H I}) = 17.5 - 18.7$ , and for two different Doppler parameters,  $b(\text{H I}) = 9.08 \text{ km s}^{-1}$  and  $b(\text{H I}) = 12.85 \text{ km s}^{-1}$ . With only a few exceptions, the range of column densities covers the values observed for the  $d < 100 \text{ pc}$  lines of sight listed in Table 1. The two Doppler parameters represent temperatures of  $T = 5000 \text{ K}$  and  $T = 10,000 \text{ K}$ , respectively (in the absence of nonthermal broadening), which roughly define the range of temperatures that are generally observed in the local ISM (see §4.4).

In Figure 5, the D I line is clearly narrower for the lower  $b$  value, and at low column densities the Doppler core of the H I absorption is also narrower, but the far damping wings of the H I absorption are only dependent on the column density. At the highest column densities shown, the Doppler core of the H I absorption has been obliterated by the broadening absorption from the damping wings, so nearly all dependence on  $b$  is lost. By  $\log N(\text{H I}) = 18.7$ , the D I absorption has become saturated and almost completely blended with H I. Thus, the D I line is no longer very useful for constraining  $N(\text{H I})$  via the  $\text{D}/\text{H} = 1.5 \times 10^{-5}$  assumption. However, the width of the base of the H I absorption has become much more sensitive to  $N(\text{H I})$ , so a reasonably accurate H I column density can still be measured in this high column regime.

The ISM velocity structure along a line of sight is something that we take into account in our Ly $\alpha$  fits, when this information is available. Unfortunately, the thermal width of the D I line is too large to suggest the presence of any but the most widely separated ISM components, and the H I absorption is naturally far too broad and opaque for these purposes. The ISM Mg II h & k absorption lines are the most commonly used lines for studying the velocity structure of the local ISM, although weaker Fe II lines observable in near-UV spectra can be useful as well. The large atomic weights of the Mg II and Fe II species mean that the thermal broadening of their ISM absorption lines is much lower than for D I and H I. In fact, these lines are typically dominated by nonthermal rather than thermal broadening. Thus, when observed at the highest spectral resolution accessible to GHRS or STIS, the very narrow Mg II and Fe II lines are ideal for indentifying multiple ISM velocity components.

Table 1 indicates which of our lines of sight have high resolution Mg II data that can be used to infer the ISM velocity structure. Redfield & Linsky (2002, hereafter RL02) have already analyzed these and other data to provide a complete survey of observed ISM Mg II and Fe II absorption for lines of sight within 100 pc. In cases where multiple ISM components are seen, we use the results of RL02 to constrain multi-component fits to our Ly $\alpha$  data. In a multi-component Ly $\alpha$  fit we force the velocity separations of the components to be the same as those seen for Mg II. We do not fix the velocities themselves in order to allow the fit to account for possible differences in the



wavelength calibrations of the Mg II and Ly $\alpha$  spectra, so we allow one component centroid to vary and force the other components to have the appropriate shifts from that component. Because the ISM components are so highly blended in the broad H I and D I lines, our philosophy is to initially assume as many constraints as possible. Thus, initially we force all components to have the same Doppler parameter in our fits (though we do not force a particular value), and we also assume that the column density ratios of the individual components are the same as found for Mg II. If a reasonable fit to the data cannot be obtained with these constraints we try relaxing them, the justification being that warm, neutral material within the Local Bubble is not entirely homogeneous. Temperatures and dust depletions within the local ISM vary to some extent, resulting in variations in Doppler parameters and Mg II/H I column density ratios (Piskunov et al. 1997; Redfield & Linsky 2004b). However, all components are always constrained by the deuterium-hydrogen self-consistency requirements described above.

Note that throughout this paper, the “reasonableness” of a fit is ultimately assessed by eye. The fitting process includes the tweaking of the assumed stellar emission profile to maximize the quality of a fit (see above). Since this tweaking is not automated, the final value of  $\chi^2$  is in large part dependent on our ability to alter the Ly $\alpha$  profile in a reasonable fashion. This ability is imprecise and hard to quantify, so the final value of  $\chi^2$  is of limited usefulness in assessing whether a fit is acceptable, or whether it is necessary to relax certain assumptions in order to obtain a better fit. Thus, we ultimately rely on our own subjective judgment rather than using a certain  $\chi^2$  threshold or some other statistical test.

For 25 of the 33 lines of sight, we are able to adequately fit the Ly $\alpha$  spectra with only ISM absorption. The resulting fits are shown in Figure 6 along with the reconstructed stellar Ly $\alpha$  profiles. Only the total ISM absorption is shown in Figure 6. For the multi-component fits, Figure 3 provides an idea of what the absorption contributions from the individual components are like. (Although the Figure 3 fits are D I-only fits, the H I+D I fits in Figure 6 will not be very different in how they fit the D I line due to the constraints described above that are imposed on these fits.)

Table 2 lists the parameters of these fits, using the ID numbers assigned in Table 1 to identify the stars. The quoted  $1\sigma$  uncertainties indicate only the random errors induced in the fits by the noise of the spectra. There is no attempt to include systematic errors such as those associated with the shape of the assumed stellar line profile, which surely dominate the uncertainty in the analysis.

For the H I column densities, which are of particular interest for ISM studies, systematic errors include uncertainties in the assumed D/H value, keeping in mind that for most of our lines of sight the dominant constraint on  $N(\text{H I})$  is  $N(\text{D I})$ . The uncertainties in the average Local Bubble D/H values quoted near the beginning of this section are  $\sim 5\%$ . When combined with uncertainties related to the reconstructed stellar line profile and the ISM velocity structure, we believe that typical uncertainties in the *total* H I column densities listed in Table 1 are  $\sim 10\%$ , or about 0.04 dex in  $\log N(\text{H I})$ . (See the notes on the  $\xi$  Boo analysis in §4.5 for discussion on how such errors might affect detection of heliospheric and astrospheric absorption.) However, in cases where a good

D I profile is not present in the data, either due to poor S/N or a high column density that leads to D I being saturated and blended with H I (e.g., HD 203244, HD 106516, HD 128987, HD 28568, HD 28205, HD 28033, HD 209458, and  $\iota$  Cap), systematic uncertainties in the  $\log N(\text{H I})$  values listed in Table 1 are probably more like 0.1 – 0.2 dex.

It should be noted that in multi-component cases, the total H I column density along a line of sight will be known better than the column densities of the individual components, which are listed in Table 2, because the components are so highly blended that the component H I column densities will be highly dependent on the assumptions made about the components described above. Thus, systematic errors for the  $\log N(\text{H I})$  values listed in Table 2 for the individual components will be even higher than those estimated above for the total H I column densities. For the multi-component fits, the component numbers listed in Table 2 are the same numbers as those used by RL02. The last column of Table 2 indicates which lines of sight are discussed in more detail in §4.5.

There are three different velocities listed in Table 2 that can be compared with the measured ISM velocity,  $v(\text{H I})$ :  $V_{LIC}$ ,  $V_G$ , and  $v(\text{Mg II})$ . The  $V_{LIC}$  quantity indicates the line-of-sight velocity predicted by the Local Interstellar Cloud (LIC) vector (Lallement & Bertin 1992; Lallement et al. 1995), which is pointed towards Galactic coordinates [ $l = 186.1^\circ$ ,  $b = -16.4^\circ$ ] with a magnitude of  $25.7 \text{ km s}^{-1}$ . This agrees well with measurements of ISM particles moving through the solar system, which suggest a flow directed at coordinates [ $l = 183.3^\circ$ ,  $b = -15.9^\circ$ ] at a speed of  $26.3 \text{ km s}^{-1}$  (Witte et al. 1993; Witte 2004). However, for lines of sight near the Galactic center direction, the so-called G cloud vector of Lallement & Bertin (1992) can be a better predictor of ISM absorption line velocities, so the  $V_G$  quantity indicates the velocities suggested by this vector. A sky map from Linsky et al. (2000) provides a crude estimate of the region on the sky where the G cloud vector is applicable, which suggests that the G cloud vector is most likely to apply for stars 33, 39, 45, 46, and 52. It is worth noting that it is very questionable whether the G cloud is truly distinct from the LIC and other nearby clouds, or if the apparent different velocity vector in that direction is merely a product of complex velocity gradients within local ISM material (Frisch, Grodnicki, & Welty 2002; Frisch 2003). Despite this ambiguity, the G cloud vector is still useful for our purposes as a predictor of ISM velocities in directions where the LIC vector clearly does not work. Finally, for lines of sight that have Mg II measurements, we also list in Table 2 the Mg II velocities from RL02,  $v(\text{Mg II})$ , although for  $v$  Peg and  $\iota$  Cap we choose to quote the Fe II velocities instead (see §4.5).

### 4.3. Identifying the Presence of Heliospheric and/or Astrospheric Absorption

The null assumption in all our Ly $\alpha$  analyses is that there is no heliospheric or astrospheric absorption present. We make every effort to find a reasonable fit to the H I+D I Ly $\alpha$  absorption assuming the presence of only ISM absorption. However, for 8 of our 33 lines of sight we conclude that there is simply no way that the D I and H I absorption can be fitted in a self-consistent manner without including additional H I absorption beyond that from the ISM. The additional H I

absorption component must have a column density too low [ $\log N(\text{H I}) < 17.0$ ] to produce any absorption in lines from much less abundant species such as D I, Mg II, or Fe II. It is this excess H I absorption that we interpret as being from the heliosphere or from the astrospheres surrounding the observed stars.

In our fits to these data in Figure 7, we add a single absorption component to the analysis to represent heliospheric and/or astrospheric absorption. This component is labeled as “HS/AS” in Table 2, where the final fit parameters are listed for all our Ly $\alpha$  fits. In Figure 7, we show the absorption provided only by the ISM, the discrepancy with the data indicating the excess absorption that we believe must be coming from HS/AS absorption. Past theoretical work has shown that the heliosphere only produces excess absorption on the red side of the Ly $\alpha$  absorption line, while astrospheric absorption produces excess absorption on the blue side of the line (Gayley et al. 1997; Izmodenov, Lallement, & Malama 1999b; Wood, Müller, & Zank 2000c). The redshift of heliospheric absorption relative to the ISM is mostly due to the deceleration and deflection of H atoms as they cross the bow shock, whereas the corresponding effect for astrospheres results instead in a blueshift since our perspective is from outside the astrosphere rather than inside. Thus, based on the fits in Figure 7, we report and list in Table 1 the following new astrospheric absorption detections: EV Lac, 70 Oph,  $\xi$  Boo, 61 Vir,  $\delta$  Eri, HD 128987, and DK UMa. However, we consider the 61 Vir and DK UMa detections to be marginal (see §4.5). The new heliospheric absorption detections are: 70 Oph,  $\xi$  Boo, 61 Vir, and HD 165185.

Details about the evidence for the presence of the HS/AS absorption will be provided in §4.5 for each individual line of sight, but some general comments can be made here. The most important one is that it is impossible to overstate the importance of the constraints on the ISM H I absorption provided by the D I absorption. In cases where only heliospheric *or* astrospheric absorption is present (EV Lac,  $\delta$  Eri, HD 165185, HD 128987, and DK UMa), the HS/AS absorption produces a significant shift of the H I absorption centroid away from that suggested by the D I absorption (see Fig. 7). If multiple ISM components are present, one can try to account for this by allowing the ISM components to have different Doppler parameters. Given the saturated nature of the H I absorption, increasing  $b(\text{H I})$  for one component can significantly increase the absorption in this component relative to the others, whereas this will not be the case for the unsaturated D I line, which is far more affected by the relative column densities of the components than by their relative  $b(\text{D I})$  values. Multiple ISM components can therefore in principle induce an apparent shift of the H I absorption relative to D I. However, because the ISM absorption components are always so highly blended, and because of the stringent deuterium-hydrogen self-consistency constraints described in §4.2, the relative velocity shift that can be induced in this fashion without resulting in poor fits to either D I or H I is limited.

A second source of evidence for HS/AS absorption, especially important in cases where *both* heliospheric and astrospheric absorption are present (70 Oph,  $\xi$  Boo, and 61 Vir), is the overall width of the base of the H I absorption. The presence of HS/AS absorption makes this width larger than can be explained by ISM absorption alone (see Fig. 7). In the H I column density regime of

concern here, one can try to broaden an ISM H I component either by increasing  $b(\text{H I})$  or  $N(\text{H I})$ . However the  $\text{D}/\text{H} = 1.5 \times 10^{-5}$  constraint means that it is not possible to greatly increase  $N(\text{H I})$  without producing too much D I absorption, and the  $b(\text{H I}) = \sqrt{2}b(\text{D I})$  constraint means that increasing  $b(\text{H I})$  too much will eventually make the D I absorption too broad.

In principle, the stellar Ly $\alpha$  profiles can be altered to account for the excess HS/AS absorption in Figure 7, but this does not work in practice since the alterations necessary to remove the need for the HS/AS absorption yield profiles that are completely implausible (Wood, Alexander, & Linsky 1996a). Using  $\delta$  Eri as an example, changing the stellar profile to fit the data without requiring the existence of the excess H I absorption seen in Figure 7 necessitates the assumption of a profile that decreases from about where it is in Figure 7 at 1215.45 Å ( $\sim 9 \times 10^{-12}$  ergs cm $^{-2}$  s $^{-1}$  Å $^{-1}$ ) down to zero flux at about 1215.57 Å. This is not a reasonable stellar profile. Reasonable alterations to stellar profiles do not include the introduction of extreme profile slopes or zero flux within the emission profile.

Note that although we list the parameters for the HS/AS components in Table 2 for completeness, they are of little use in estimating properties of the heliospheric and/or astrospheric gas. More sophisticated analyses of this excess absorption using hydrodynamic modeling of the heliosphere and astrospheres is required to extract meaningful quantitative information from the heliospheric and astrospheric absorption (Wood et al. 2000c, 2002b), which will be done in a future paper. We do not bother using separate heliospheric and astrospheric absorption components even when both are clearly present, partly because of the limited usefulness of the fit parameters of these empirical absorption components, and partly because our goal here is simply to infer the presence of the HS/AS absorption and illustrate the amount of excess absorption in Figure 7.

#### 4.4. The ISM Fit Parameters

The fit parameters listed for the ISM absorption components in Table 2 provide useful diagnostics for the local ISM. The column densities indicate the average ISM H I densities along the lines of sight when divided by the target distances, the velocities provide information on the ISM flow vector, and the Doppler parameters indicate the temperature of the gas, which can be estimated by the equation  $T = 60.6b(\text{H I})^2$  if the small contributions of turbulent velocities to the line broadening are neglected (Redfield & Linsky 2004b). However, interpreting the meaning of these measurements is somewhat problematic unless the velocity structure is known. The high resolution Mg II and Fe II spectra that provide this information are only available for 12 of our 33 lines of sight. Since 7 of these 12 sight lines show multiple ISM components, the prevalence of multiple velocity components is clear. The presence of unresolved velocity structure can shift the centroid of the ISM absorption away from the expected  $V_{LIC}$  or  $V_G$  values, and it can also broaden the absorption lines, thereby artificially increasing the D I and H I Doppler parameters.

Of the 12 lines of sight with Mg II and/or Fe II information, all but one show an absorption

component within  $3 \text{ km s}^{-1}$  of the expected  $V_{LIC}$  or  $V_G$  values, the exception being AU Mic (star #39). This comparison is valid whether the measured velocities considered are  $v(\text{H I})$  or  $v(\text{Mg II})$ , with the exception of  $\iota$  Cap, for which the  $v(\text{H I})$  velocities are poorly constrained and therefore discrepant (see §4.5). Of the 21 lines of sight without the benefit of the Mg II or Fe II data, 10 show line centroids over  $3 \text{ km s}^{-1}$  from the expected  $V_{LIC}/V_G$  values. The worse agreement for these sight lines is surely due to unresolved velocity structure, especially considering that the  $b(\text{H I})$  values for 7 of these 10 lines of sight are suspiciously high based on previous work. Previous analyses of high resolution HST spectra, constrained by knowledge of the ISM velocity structure, have generally suggested that warm, partially neutral clouds within the Local Bubble typically have temperatures of  $T = 5000 - 10,000 \text{ K}$ , corresponding to Doppler parameters of  $b(\text{H I}) = 9.1 - 12.8 \text{ km s}^{-1}$  (Dring et al. 1997; Piskunov et al. 1997; Wood & Linsky 1998; Redfield & Linsky 2004b). Thus, Doppler parameters of  $b(\text{H I}) > 12.8 \text{ km s}^{-1}$  are suggestive of possible unresolved velocity components. (See the notes on the AD Leo analysis in §4.5 for an example of how unresolved velocity structure can artificially increase measured Doppler parameters.)

One issue that should be mentioned is that the  $b(\text{H I})$  values reported in Table 2, which are derived from the H I+D I fits, are almost always  $1 - 2 \text{ km s}^{-1}$  larger than those that we measure from the D I-only fits [assuming  $b(\text{H I}) = \sqrt{2}b(\text{D I})$ ], such as the fits shown in Figure 3. The most likely explanation for this is that the LSF we are assuming is slightly broader than it should be, meaning that we are overcorrecting for instrumental broadening. For the two single-component fits in Figure 3 ( $\xi$  Boo and DK UMa), the difference between the pre- and post-convolution fits indicates the extent that the D I absorption profile is unresolved based on our assumed LSF. The D I line is clearly not entirely resolved in the E140M data, which means that the convolution correction is important and that uncertainties in the LSF will lead to uncertainties in the fit parameters, especially  $b(\text{D I})$ . This emphasizes the importance of high spectral resolution in the  $\text{Ly}\alpha$  analyses.

Finally, since we are *a priori* assuming a D/H value in our fits, our analysis cannot refine the value of the Local Bubble D/H ratio, but we can at least say that our success in fitting the data in Figures 6 and 7 indicates that the  $\text{Ly}\alpha$  data analyzed here are all consistent with the assumed value of  $\text{D}/\text{H} = 1.5 \times 10^{-5}$ .

#### 4.5. Notes on Individual Lines of Sight

We here provide comments on some of the individual lines of sight that have been analyzed. These include not only notes of particular interest about the lines of sight, but also in some cases details about how multiple ISM components were constrained and especially the precise evidence for heliospheric and astrospheric absorption, when present. The comments frequently refer to information listed in Tables 1 and 2.

**AD Leo (#31):** This line of sight is notable for having a remarkably high ISM H I column density,  $\log N(\text{H I}) = 18.47$ , given its very short distance of 4.69 pc. The implied average

density of  $n(\text{H I}) = 0.204 \text{ cm}^{-3}$  is to our knowledge the highest average density yet measured for any line of sight within 100 pc (i.e., within the Local Bubble), being slightly above the  $n(\text{H I}) = 0.199 \text{ cm}^{-3}$  value towards HD 82558 (see Table 1). The large  $b(\text{H I})$  value of the fit and the discrepancy between  $v(\text{H I})$  and the expected  $V_{LIC}$  velocity strongly imply the presence of multiple ISM components. There are no high resolution Mg II spectra available to verify this, but in Figure 8 we show an alternative fit to the data where an arbitrary second ISM component is included. The second component is assumed to be redshifted by  $12 \text{ km s}^{-1}$  from the primary component, with a column density a factor of 10 lower than that of the primary component. The Doppler parameters of the two components are forced to be identical, and in the fit the Doppler parameter of both components ends up at  $b(\text{H I}) = 12.85 \text{ km s}^{-1}$ . This is a more plausible result than the high  $b(\text{H I}) = 14.05 \text{ km s}^{-1}$  value from the single component fit, illustrating how the presence of multiple components can artificially increase measured Doppler parameters. The primary reason that the Figure 6 fit has such a poor  $\chi^2$  value ( $\chi^2_\nu = 2.571$ ) is the very high signal-to-noise (S/N) of the data. The high S/N is a result of the unusually long 52 ksec exposure time of the coadded HST spectrum, which was taken as part of an extensive flare monitoring campaign (Hawley et al. 2003).

**EV Lac (#32):** Figure 7 shows that there is a lot of excess H I absorption on the blue side of the line, resulting in the centroid of the H I absorption being highly blueshifted with respect to the D I absorption. This therefore represents a convincing detection of astrospheric absorption.

**70 Oph (#33):** The Mg II analysis by RL02 suggests a complex line of sight with 3 ISM components, including a component (component 3 in Table 2) that is shifted relative to the primary component by an unusually large amount for such a short sight line. The primary component (component 1) is a G cloud component. The complexity of the ISM structure complicates the Ly $\alpha$  analysis. In fitting D I by itself (see Fig. 3), we find that we cannot fit the data well enough while forcing the column density ratios of the 3 components to be consistent with those of the Mg II fit, so in Figure 3 we have allowed the column density ratios to be different. This D I fit predicts a Doppler parameter for the H I absorption of  $b(\text{H I}) = 8.4 \pm 0.9 \text{ km s}^{-1}$  [assuming as always  $b(\text{H I}) = \sqrt{2}b(\text{D I})$ ], implying a very low ISM temperature of  $T = 4300 \pm 900 \text{ K}$ , consistent with the results of Redfield & Linsky (2004b). This measurement is not implausible since other G cloud lines of sight have also shown particularly low temperatures (Linsky & Wood 1996; Wood, Linsky, & Zank 2000b; Redfield & Linsky 2004b). In the D I+H I fit shown in Figure 7 and Figure 9a we force the column density ratios to be the same as those derived from the D I-only fit. However, fits to the data with only the ISM components invariably require  $b(\text{H I}) \approx 15 \text{ km s}^{-1}$  in order to produce H I absorption broad enough to fit the data. This fit obviously produces D I absorption much too broad to fit the D I line, considering the low  $b(\text{H I}) = 8.4 \text{ km s}^{-1}$  measurement quoted above from the D I-only fit. Thus, the data require the addition of an HS/AS component in order to explain the overly broad H I absorption. The best fit in Figure 7 shows excess absorption on both sides of the line, implying the presence of both heliospheric and astrospheric absorption. Note

that because the blueshifted component 3 is not a strong contributor to the D I absorption, it is possible to allow *only* that component to have  $b(\text{H I}) \approx 15 \text{ km s}^{-1}$  while still fitting D I reasonably well. In doing so, component 3 becomes broad enough to account for the excess blue-side H I absorption, as shown in Figure 9b, meaning that only heliospheric H I absorption would be inferred from the data. However,  $b(\text{H I}) \approx 15 \text{ km s}^{-1}$  is inconsistent with the width of the Mg II line. Even in the unlikely case that the component 3 Mg II absorption line is entirely thermally broadened, the Mg II Doppler parameter of  $b(\text{Mg II}) = 2.76 \pm 0.15 \text{ km s}^{-1}$  measured by RL02 suggests an upper limit for the H I Doppler parameter of  $b(\text{H I}) < 14.3 \text{ km s}^{-1}$ , so we do not consider the fit in Figure 9b to be an acceptable interpretation of the data. Thus, we believe the astrospheric detection implied by the fit in Figure 7 is solid, as well as the heliospheric detection.

**$\xi$  Boo (#34):** Excess absorption on both sides of the Ly $\alpha$  line is indicated by the fit in Figure 7, so this is both a heliospheric and an astrospheric detection. The heliospheric absorption is slightly stronger than the astrospheric absorption, inducing a slight redshift of the total H I absorption relative to D I. Thus, the evidence for the heliospheric absorption is somewhat stronger than the evidence for the astrospheric absorption. Evidence for the astrospheric absorption relies on the relative widths of the H I and D I lines. Figure 10 shows a fit to the  $\xi$  Boo data in which the centroid of the HS/AS absorption component is fixed in such a way that it can only account for the red-side excess (i.e., the heliospheric absorption). The fit works well for H I, but the  $b(\text{H I}) = 12.7 \pm 0.2 \text{ km s}^{-1}$  value of the ISM absorption leads to a D I absorption line that is too broad. The D I-only fit in Figure 3 suggests  $b(\text{H I}) = 9.6 \pm 0.6 \text{ km s}^{-1}$ . We believe that this discrepancy is too large to be explained by the possible LSF problem noted in §4.4, so we cannot consider the fit to D I in Figure 10 to be acceptable. Thus, we conclude that the astrospheric detection implied by the Figure 7 fit is secure. Since the width of the ISM absorption depends in part on  $N(\text{H I})$  as well as  $b(\text{H I})$  (see Fig. 5), uncertainties in  $N(\text{H I})$  could potentially lead to an erroneous detection of HS/AS absorption. In §4.2, we estimate uncertainties in  $N(\text{H I})$  to be typically  $\sim 10\%$  after including systematic errors, such as uncertainties in the  $\text{D}/\text{H} = 1.5 \times 10^{-5}$  assumption. In Figure 11, we repeat the fit from Figure 7, but we also show how the ISM absorption profile changes when the H I column density is changed by 10%. A 10% increase in  $N(\text{H I})$  clearly does not come close to explaining the excess H I absorption that we believe is HS/AS absorption.

**61 Vir (#35):** The evidence for the heliospheric and astrospheric absorption shown in Figure 7 is almost identical to that for  $\xi$  Boo, so the 61 Vir analysis mirrors the  $\xi$  Boo analysis described above. However, the S/N of the 61 Vir data is not nearly as high as that of the  $\xi$  Boo spectrum. This means that the width of the D I absorption (and therefore the ISM H I absorption as well) cannot be measured with the same precision. Thus, the evidence for the astrospheric absorption is weaker, and in Table 1 we indicate only a marginal detection of astrospheric absorption.

**$\delta$  Eri (#37):** The enormous amount of excess H I absorption on the blue side of the line leads to a

large blueshift of H I relative to D I, amounting to a very convincing detection of astrospheric absorption (see Fig. 7).

**$\kappa$  Cet (#38):** This is a complex, 3 component line of sight based on the Mg II data (RL02). As is the case for 70 Oph (see above), we find that the D I absorption is fitted significantly better when the individual components are allowed to have column density ratios different from that of Mg II. Thus, the fit in Figure 3 allows the column densities of the individual components to vary, and in our H I+D I fits we force the column density ratios to be the same as for the D I-only fit. However, we are unable to fit the data with the usual assumption of equal Doppler parameters for all ISM components. In order to fit the data we allow the most blueshifted component (component 3) to have a higher Doppler parameter, which in our best fit is  $b(\text{H I}) = 13.3 \pm 0.2 \text{ km s}^{-1}$ . This is suspiciously high for local ISM material, but the  $b(\text{H I})$  value is not inconsistent with the  $b(\text{Mg II}) = 2.48 \pm 0.38 \text{ km s}^{-1}$  measurement (RL02), unlike what happens in the similar 70 Oph analysis (see above). Thus, we conclude that the fit is plausible and no HS/AS absorption component is required to fit the data.

**AU Mic (#39):** This is the one line of sight for which *both* H I and Mg II velocities imply a significant discrepancy from the values predicted by the G and LIC vectors (see Table 2). The Mg II absorption lines analyzed by RL02 do not show asymmetries that would demonstrate the presence of multiple ISM components, but both the Mg II and H I Doppler parameters,  $b(\text{Mg II}) = 4.94 \pm 0.74 \text{ km s}^{-1}$  and  $b(\text{H I}) = 13.74 \pm 0.08 \text{ km s}^{-1}$ , are suspiciously high. The Mg II spectrum analyzed by RL02 is a GHRS Ech-B spectrum taken through GHRS’s large aperture before the installation of the COSTAR corrective optics. The spectrum therefore has significantly lower resolution than is normally achievable with the high resolution gratings of GHRS and STIS. Furthermore, it is difficult to estimate the shape of the stellar Mg II profile above the ISM absorption due to the narrowness of the Mg II emission lines, and the location of the ISM absorption on the side of the line. For these reasons, we suspect that there are in fact multiple ISM components towards AU Mic that are not apparent due to these difficulties with the Mg II data. Finally, it is worth noting that a debris disk has recently been discovered around AU Mic (Kalas, Liu, & Matthews 2004; Liu 2004). Despite being edge-on, there is to our knowledge no evidence for any absorption from the disk in the UV spectra of AU Mic from HST, including the Ly $\alpha$  line analyzed here. The disk must therefore be gas-poor.

**$\zeta$  Dor (#40):** For this two-component fit, we force the velocity separations and column density ratios of the components to be the same as in the Mg II fit of RL02, but it is necessary to allow the Doppler parameters of both components to vary in order to fit the H I absorption. Component 1 ends up with a very high Doppler parameter of  $b(\text{H I}) = 14.8 \pm 0.1 \text{ km s}^{-1}$ . However, the Mg II Doppler parameter of  $b(\text{Mg II}) = 5.76 \pm 0.37 \text{ km s}^{-1}$  reported by RL02 for this component is also extremely high, so we believe that the high  $b(\text{H I})$  value is plausible.

**HD 165185 (#45):** The H I absorption shows a small but significant redshift relative to the D I absorption, indicating the presence of heliospheric absorption, as shown in Figure 7.



**HD 203244 (#46):** The  $\log N(\text{H I}) = 18.82$  column density for HD 203244 is high enough that the H I and D I absorption lines are completely blended (see Fig. 6). This line of sight and that towards HD 82558 have two of the three highest column densities listed in Table 1, despite these stars being only about 20 pc away. Since column densities this high are clearly rare within the Local Bubble, they are presumably due to relatively small clouds that few sight lines pass through. In order to explain the high columns, these small clouds must necessarily have average densities that are significantly higher than the  $n(\text{H I}) \approx 0.1 \text{ cm}^{-3}$  value that is typical for the LIC (Linsky et al. 2000).

**HD 106516 (#50):** A clear D I absorption line cannot be discerned in the data, partly due to poor S/N and partly due to a high H I column density that leads to D I and H I being at least partly blended. The measured H I column density of  $\log N(\text{H I}) = 18.57$  is the only fit parameter that can be trusted, and this value is probably good to only within  $\pm 0.2$  dex considering systematic errors. This is at the upper end of the range of  $N(\text{H I})$  uncertainties for our measurements quoted in §4.2.

**HD 128987 (#52):** Analogous to the EV Lac and  $\delta$  Eri lines of sight mentioned above, the HD 128987 data show extensive blue-side excess H I absorption, implying a substantial amount of astrospheric absorption (see Fig. 7). The detection is very convincing despite the rather poor S/N of the data. In the Figure 7 fit, the HS/AS component is forced to have a centroid on the blue side of the H I line to keep it from contributing absorption to the red side of the H I line. (If the resulting fit in Figure 7 had been poor, that would have been evidence for heliospheric absorption, in addition to the astrospheric absorption.)

**DK UMa (#53):** Figure 12 shows the best fit to the data possible with only ISM absorption. The fit shows a bit too much absorption on the blue side of the D I line, and slightly too little absorption on the blue side of the H I line. In other words, the H I absorption in reality seems to be slightly blueshifted relative to D I, suggesting the presence of astrospheric absorption. Thus, the best fit in Figure 7 includes an HS/AS component. The implied excess absorption is quite weak compared with the other detections of astrospheric and heliospheric absorption, but the S/N of the data is good enough for the problems with the Figure 12 fit to be considered significant. Furthermore, there are Mg II observations that show only a single ISM component towards DK UMa, which means that the deficiencies of the Figure 12 fit are not due to any effects of multiple ISM components. Thus, we consider this to be an astrospheric detection, though we consider it a marginal one, as noted in Table 1. The HS/AS component in the Figure 7 fit contributes a little absorption to the red side of the line as well as to the blue side where the astrospheric absorption resides, but the red-side contribution is too weak for us to consider that to be evidence for heliospheric absorption.

**V471 Tau (#58):** This target is a K2 V+DA eclipsing binary with a very short period of 0.51 days. The UV STIS spectrum as a whole is a continuum spectrum from the hot white dwarf star, but the white dwarf continuum decreases dramatically near  $\text{Ly}\alpha$  so that the  $\text{Ly}\alpha$  emission

line from the K2 V star contributes most of the background for the ISM Ly $\alpha$  absorption. The spectrum shown in Figure 1 is the result of a coaddition of spectra taken at different orbital phases, which we do in order to provide sufficient S/N for our analysis. Since the ISM absorption is stationary in the individual exposures, the coaddition is valid for our purposes despite the fact that the overlying Ly $\alpha$  profile of the K2 V star moves due to the rapid orbital motion. The nonstationary emission results in a reconstructed line profile in Figure 6 that looks strange and is in fact unphysical, but an average integrated stellar Ly $\alpha$  line flux can still be estimated from it (see §7). Variable ultraviolet absorption features in *International Ultraviolet Explorer* (IUE) and GHRIS spectra have been interpreted as being due to coronal mass ejections (CMEs) from the K2 V star, with an implied mass loss rate much higher than that of the Sun (Mullan et al. 1989; Bond et al. 2001). We see no astrospheric H I absorption that would provide additional evidence for a strong wind from V471 Tau. This by no means disproves the CME interpretation of the variable UV features, given the likely possibility that V471 Tau is surrounded by a fully ionized ISM that will produce no astrospheric H I absorption regardless of the stellar mass loss rate (see §6).

**HD 209458 (#59):** This star has a planetary companion that transits in front of the star once every 3.52 days (Charbonneau et al. 2000). By comparing STIS G140M Ly $\alpha$  spectra taken during and outside transit times, Vidal-Madjar et al. (2003) find that the Ly $\alpha$  profile decreases as much as 15% at some wavelengths during transit, suggesting absorption from an extended, evaporating planetary atmosphere. This does not affect our analysis of the ISM absorption in the E140M spectrum, however, and we are able to fit the rather noisy D I and H I absorption lines with a single ISM absorption component.

*v* **Peg (#60):** The ISM Mg II and Fe II absorption lines show three velocity components for this line of sight (RL02). Due to the saturated nature of the Mg II lines, we decide that the less opaque Fe II lines provide more precise constraints for our fits in Figures 3 and 6. Thus, the *v*(Mg II) velocities listed in Table 2 for *v* Peg are in this case the Fe II velocities. For the Ly $\alpha$  fit in Figure 6, we force the velocity separations and column density ratios of the components to be the same as Fe II, but we have to allow the Doppler parameters of the individual components to be different to acceptably fit the data. The Doppler parameters of the two weaker components (components 1 and 3) are suspiciously high (see Table 2), but they are not inconsistent with the Fe II Doppler parameters from RL02. Considering uncertainties induced by the complexity of the line of sight, we conclude that this is a reasonable fit.

**HD 32008 (#61):** This target is a G7 IV-III+DA binary according to Cutispoto et al. (1999). As is the case for V471 Tau (see above), the white dwarf dominates the UV spectrum everywhere except in the region of Ly $\alpha$ , where the emission line from the G7 IV-III star provides most of the background continuum for the ISM absorption. There are no Mg II or Fe II spectra to precisely define the ISM velocity structure of this line of sight, but inspection of the D I absorption reveals that this is one case where ISM velocity components are so widely separated that evidence for multiple components is apparent even in the broad D I line (see Fig. 3).

Thus, in Figure 3 D I is fitted with two components. The H I+D I fit in Figure 6 is likewise performed with two components, where we force them to have the same Doppler parameters, but allow their velocities and column densities to both vary.

**$\iota$  Cap (#62):** Three ISM velocity components are suggested by the Mg II and Fe II absorption lines (RL02). As is the case for  $\nu$  Peg (see above), the Mg II lines are saturated, so we decide to use the less opaque Fe II lines to constrain the fit in Figure 6. Thus, the  $v(\text{Mg II})$  velocities listed in Table 2 for  $\iota$  Cap are actually Fe II velocities. The H I column density for this line of sight,  $\log N(\text{H I}) = 18.70$ , is high enough that D I is nearly saturated and is almost completely blended with the H I absorption. This blending and the complexity of the line of sight make the analysis poorly constrained and very uncertain. We believe that the large H I Doppler parameters,  $b(\text{H I}) = 15.9 \text{ km s}^{-1}$ , and the large discrepancies between the  $v(\text{H I})$  and  $v(\text{Mg II})$  velocities in Table 2 are a consequence of these difficulties and the discrepancies should therefore be regarded with skepticism.

## 5. THE HELIOSPHERIC ABSORPTION DETECTIONS

The 33 new lines of sight that we have analyzed have resulted in 4 new detections of heliospheric Ly $\alpha$  absorption. This brings the total number of detections to 8, if one considers the Alpha/Proxima Cen detections as a single line of sight. This is a large enough number that we can investigate what the lines of sight that produce detectable absorption have in common. There are really only two factors that determine whether a line of sight will have detectable heliospheric Ly $\alpha$  absorption. One is the ISM H I column density, since a high ISM column will mean a broad absorption line that will hide the heliospheric absorption. The second factor is the orientation of the line of sight through the heliosphere. This orientation is most simply described by the angle,  $\theta$ , between the line of sight and the upwind direction of the ISM flow seen by the Sun. This upwind direction has Galactic coordinates of  $l = 6.1^\circ$ ,  $b = 16.4^\circ$  (Lallement et al. 1995).

In Figure 13, we plot the ISM column densities,  $\log N(\text{H I})$ , versus  $\theta$  for all the HST-observed lines of sight listed in Table 1. Different symbols are used to indicate which lines of sight have detectable heliospheric absorption and which do not. The detections are nicely separated from the nondetections in this parameter space. As expected, the lines of sight that yield detections tend to have low  $N(\text{H I})$  values. It is also clearly easier to detect heliospheric absorption in upwind directions ( $\theta < 90^\circ$ ) than in downwind directions ( $\theta > 90^\circ$ ). Models of the heliosphere can explain this behavior quite nicely. It is in upwind directions that the heliospheric H I suffers the strongest deceleration at the bow shock (Baranov & Malama 1993, 1995; Zank et al. 1996; Wood et al. 2000c). Thus, the heliospheric absorption in these directions will be shifted away from the ISM absorption to the greatest extent, making it easier to detect. The success of the models in explaining the detection tendencies illustrated in Figure 13 is additional strong evidence that heliospheric absorption is indeed the correct interpretation for the red-side excess Ly $\alpha$  absorption.

For the upwind directions, heliospheric absorption is only detected when  $\log N(\text{H I}) < 18.2$ , but in downwind directions a detection requires  $\log N(\text{H I}) < 17.8$ . There simply are not many lines of sight that will have interstellar column densities of  $\log N(\text{H I}) < 17.8$ . Thus, the downwind detection of heliospheric absorption towards Sirius may forever remain unique (Izmodenov et al. 1999b).

The properties of a line of sight through the heliosphere are described entirely by the angle  $\theta$  only if the heliosphere is precisely axisymmetric. However, significant deviations from axisymmetry are possible due to latitudinal solar wind variations, an ISM magnetic field that is skewed with respect to the ISM flow direction, or unstable MHD phenomena near the plane of the heliospheric current sheet (Pauls & Zank 1997; Ratkiewicz et al. 1998; Opher et al. 2003). There are now enough heliospheric absorption detections to conduct at least a crude investigation into whether there is evidence for any such asymmetries, and this will be a project for the near future.

## 6. THE ASTROSPHERIC ABSORPTION DETECTIONS

The 7 new astrospheric detections found here bring the total number of detections up to 13. The astrospheric detections are primarily of interest because the astrospheric absorption provides a diagnostic for stellar winds that are otherwise completely undetectable. Mass loss rates have been measured for all of the older detections, and these measurements have been used to infer how winds vary with age and activity for solar-like main sequence stars (Wood et al. 2002b). We are currently measuring mass loss rates using the new astrospheric detections, but these results will have to wait for a future paper.

We can use the new detections to investigate what is common among the lines of sight that have detections, as we did for the heliospheric detections in §5, but the situation is more complicated in the case of astrospheres. There are many more factors involved in the detectability of the astrospheric absorption, including the nature of the ISM surrounding the star, the total integrated ISM H I column density for the line of sight, the speed and orientation of the ISM flow vector seen by the star, and the properties of the stellar wind. A nondetections of astrospheric absorption could be due to any number of these factors, so it is generally impossible to use nondetections of astrospheric absorption to infer anything about the stellar wind or surrounding ISM, unlike what can be done with the nondetections of heliospheric absorption (see §5).

In Figure 14, we plot the ISM column density versus stellar distance for all of the HST-observed lines of sight listed in Table 1. The HST data points are placed into three categories: lines of sight that yield detections of astrospheric absorption, lines of sight that yield nondetections, and other lines of sight for which a search for astrospheric absorption is not appropriate due to a hot star target or low spectral resolution (see §2). Finally, for completeness we also include in Figure 14 five additional data points that are based on H I column density measurements from the *Extreme Ultraviolet Explorer* (EUVE) or *Copernicus*. These lines of sight are WD 1634-573 (Wood et al.

2002a), WD 2211-495 (Hébrard et al. 2002), WD 0621-376 (Lehner et al. 2002),  $\alpha$  Vir (York & Rogerson 1976), and  $\alpha$  Cru (York & Rogerson 1976).

Considering only those HST lines of sight for which a valid search for astrospheric absorption can be made, the detection rate is quite high within 10 pc, with 10 of 17 independent sight lines producing detections for a detection rate of 58.8%. The situation worsens dramatically beyond 10 pc, with only 3 of 31 lines of sight yielding detections, for a detection rate of only 9.7%. Furthermore, 2 of the 3 detections beyond 10 pc are considered only marginal detections (see Table 1).

There are two reasons for the distance dependence of astrospheric detectability. One is simply that longer lines of sight tend to have higher ISM column densities, as shown by Figure 14. This means that the ISM H I Ly $\alpha$  absorption will be broader, which can hide the astrospheric absorption. A second major problem with more distant targets is that there is a high probability that they will be surrounded by hot, ionized ISM material with no neutrals, which will therefore inject no H I into the astrospheres to produce Ly $\alpha$  absorption. The Local Bubble is believed to be mostly filled with this ionized material (e.g., Sfeir et al. 1999; Lallement et al. 2003). There are regions of warm, partially neutral material embedded within the Local Bubble, and it just so happens that the Sun is located within one of these regions, explaining why even the nearest lines of sight have substantial H I column densities (see Table 1). However, the further a star is from the Sun, the more likely it will be located in the more prevalent ionized ISM. This is evident in Figure 14, which shows that H I column densities do not increase much beyond 10 pc, and average H I densities therefore decrease.

Since an astrospheric detection requires the presence of neutral material in the ISM surrounding the observed star, a detection of astrospheric absorption represents an *in situ* detection of neutral ISM at the star’s location. Thus, the astrospheric detections can in principle be used to crudely map out locations of warm, partially neutral clouds embedded within the Local Bubble. The 58.8% detection fraction within 10 pc suggests that neutral clouds occupy about 58.8% of space within 10 pc, although in reality this is really just a lower bound since nondetections of astrospheres can be for many reasons other than an ionized surrounding ISM (see above). It must also be noted that the observed targets are preferentially nearby rather than being randomly distributed throughout the volume of space within 10 pc, so the filling fraction lower limit of 0.588 is biased towards shorter distances. Nevertheless, these results clearly suggest that most of the ISM within 10 pc is warm, partially neutral gas, which is atypical within the Local Bubble.

Various observations of ISM H I atoms flowing through the heliosphere provide estimates of the H I density immediately surrounding the Sun. These estimates are typically  $n(\text{H I}) \approx 0.2 \text{ cm}^{-3}$  (Quémerais et al. 1994; Izmodenov et al. 1999a; Frisch & Slavin 2003). Except for the new measurement towards AD Leo (see §4.5), average line-of-sight densities within 10 pc are always well below this value (see Fig. 14), so crude models of the distribution of gas in the very local ISM have typically assumed instead  $n(\text{H I}) = 0.1 \text{ cm}^{-3}$  (Linsky et al. 2000; Redfield & Linsky 2000).

Most of the 10 pc lines of sight shown in Figure 14 have densities even lower than this, including most of the astrospheric detections.

Of particular interest is the  $\xi$  Boo line of sight. The Mg II absorption data show only a single velocity component, with a velocity consistent with the LIC vector (RL02). Since  $\xi$  Boo is an astrospheric detection, that would suggest that the LIC must extend the entire 6.70 pc distance towards  $\xi$  Boo, but this means that the LIC would have an average density of only  $n(\text{H I}) = 0.040 \text{ cm}^{-3}$  for this sight line, much lower than the  $n(\text{H I}) \sim 0.2 \text{ cm}^{-3}$  value measured for the LIC at the Sun’s location. Photoionization models of the LIC predict that hydrogen ionization should increase and the H I density therefore decrease towards the edge of the cloud due to less shielding from ionizing radiation (e.g., Slavin & Frisch 2002), but not to the extent that one would expect to see *this* large a decrease in an *average* line-of-sight density. There are two alternative explanations for the low average density. It is possible that there are in fact two separate clouds along the line of sight that just happen to have the same projected velocity, in which case a sizable gap in between the clouds could explain the low average density. Such a situation must be the case for DK UMa if its marginal astrospheric detection is to be believed. Only a single LIC Mg II absorption component is observed towards DK UMa (RL02), but there is no way that the LIC extends the 32.4 pc distance to that star. The second explanation is that the LIC has a substantial amount of subparsec scale patchiness, with the Sun being located within a small, high-density patch. Both of these two explanations indicate that the ISM velocity structure information provided by Mg II and Fe II absorption data may not be sufficient to infer the true character of the LIC and other very nearby interstellar material.

It is worth noting that everything said above about the  $\xi$  Boo sight line also applies to the 36 Oph sight line, except that the G cloud vector applies towards 36 Oph instead of the LIC vector. Both  $\alpha$  Cen and 36 Oph are G cloud lines of sight with astrospheric detections and with Mg II spectra that show only a single G cloud component. However, the implied average H I densities towards these stars are very different:  $n(\text{H I}) = 0.098 \text{ cm}^{-3}$  and  $n(\text{H I}) = 0.038 \text{ cm}^{-3}$ , respectively. Thus, the nearby ISM in the direction where the G cloud vector applies appears to be just as inhomogeneous as the  $\xi$  Boo line of sight, despite the apparent simplicity of the Mg II velocity structure.

With only 3 astrospheric detections beyond 10 pc, and with 2 of them being marginal detections, it is harder to infer general properties of the ISM beyond 10 pc from these results. The low detection fraction is a serious problem for potential observational searches for astrospheric absorption beyond 10 pc. In addition to our desire to use astrospheres to probe the ISM beyond 10 pc, the stellar wind research would also benefit from more distant detections, since there are many classes of stars that do not have many representatives within 10 pc. If the goal is to investigate what astrospheric absorption and stellar winds are like for giants or young, solar-like G stars, for example, it is necessary to look beyond 10 pc to find targets. If astrospheres could be detected from the ground, an extensive observing program could be proposed and a low 5 – 10% detection fraction tolerated, but this is not practical when the only instrument capable of detecting the as-

trospheres is the UV spectrograph on board HST. For the time being, this point may be moot. The apparent recent demise of the STIS instrument in 2004 August means that no new high resolution Ly $\alpha$  spectra will be possible for the foreseeable future.

## 7. CHROMOSPHERIC Ly $\alpha$ FLUXES

The H I Ly $\alpha$  line is one of the strongest and most important emission lines from the upper chromospheres of cool stars. However, the very strong ISM absorption that is always present in observations of this line makes measuring reliable line fluxes difficult (Landsman & Simon 1993). In order to measure an accurate line flux, a high resolution spectrum must be obtained that resolves the line profile, and then the intrinsic stellar profile must be reconstructed using the kind of time-consuming analysis technique described in §4. Due to these complications, more attention has been given to other chromospheric diagnostics, such as the Mg II h & k lines. Since relatively little has been done with Ly $\alpha$  measurements in the past, we believe it is worthwhile to see how our ISM-corrected Ly $\alpha$  fluxes correlate with other, more popular activity diagnostics.

We use the reconstructed Ly $\alpha$  profiles shown in Figures 6 and 7 to measure integrated Ly $\alpha$  fluxes for our stars, and these fluxes are listed in Table 3 (in ergs cm $^{-2}$  s $^{-1}$ ), along with fluxes measured from previously analyzed data (see references in Table 1). For Capella (#13) and HR 1099 (#21), the fluxes are divided between the two unresolved stars of these binaries. The division was made during the absorption analysis for Capella (Linsky et al. 1995a), while for HR 1099 we assume the division between the stars is the same for Ly $\alpha$  as it is for the Mg II lines (Wood et al. 1996b). Many of the Ly $\alpha$  profiles in Figures 6 and 7 have self-reversals near line center. This is due to the frequent use of the Mg II h & k lines to provide an initial guess for the shape of the Ly $\alpha$  profile. However, it should be emphasized that the exact line shape should not be considered to be terribly precise, especially the parts of the line profile that lie above the saturated H I absorption core where the data provide absolutely no information on the profile. Uncertainties in the integrated line fluxes in Table 3 will generally be larger for the lines of sight with higher ISM column densities since the correction for absorbed flux will generally be higher in those cases, but a typical average error for the fluxes in Table 3 is of order 20%.

Coronal X-ray and chromospheric Mg II fluxes are also listed in Table 3 for comparison with the Ly $\alpha$  fluxes. The X-ray fluxes are from the *ROSAT* all-sky survey (RASS), which used the Position Sensitive Proportional Counter (PSPC) instrument. The exception is  $\chi$  Her (#43), for which a pointed PSPC observation is used since this star is undetected in the RASS. Over half the X-ray fluxes are taken from the nearby star survey of Schmitt & Liefke (2004). The bright and giant star RASS surveys of Hünsch, Schmitt, & Voges (1998a,b) provide many additional fluxes. Measurements for three of the Hyades stars (#55–#57) are from Stern, Schmitt, & Kahabka (1995). For four stars (#18, #19, #25, and #52), we compute a flux ourselves from the RASS count rate listed in the HEASARC database and an assumed conversion factor of  $6 \times 10^{-12}$  ergs cm $^{-2}$  ct $^{-1}$ . The white dwarf companions of V471 Tau (#58) and HD 32008 (#61) presumably dominate their

X-ray fluxes, so no fluxes are listed in Table 3 for these stars.

Many binaries are not resolved in *ROSAT* PSPC observations, making it impossible to know how to divide the X-ray flux among the individual stars. For the  $\alpha$  Cen and 61 Cyg binaries, *ROSAT* High Resolution Imager (HRI) observations that resolve the binaries are used to determine how to divide the RASS X-ray fluxes among the stars in Table 3 (Schmitt & Liefke 2004). For Capella (#13), we assume the relative contributions of the two stars to the coronal Fe XXI  $\lambda$ 1356 line (Linsky et al. 1998) are applicable to the coronal X-ray flux as well. For HR 1099 (#21) and  $\xi$  Boo (#34), the emission is known to be dominated by the primary stars of these binaries, so we simply assign all the X-ray flux to those stars. Finally, we have recently used the *Chandra* X-ray telescope to resolve the 70 Oph (#33) and 36 Oph (#10) binaries. These data will be discussed in detail in a future paper, but we can report here that 70 Oph A and 36 Oph A contribute 60.4% and 58.2% of the fluxes of these binaries, respectively, so these results are used to modify the RASS fluxes in Table 3.

The Mg II fluxes in Table 3 are combined fluxes of the h & k lines. Most of the fluxes are measured from HST spectra. Although many of the ISM Mg II lines are discussed and analyzed by RL02, and some of the references in Table 1 also discuss Mg II spectra, emission line fluxes have not usually been reported so we generally have to measure these fluxes ourselves. However, we use the measurements of Linsky et al. (1995b) and Wood et al. (1996b) for Capella (#13) and HR 1099 (#21), respectively. The chromospheric Mg II emission line lies in the middle of a broad photospheric absorption line. It is difficult to know what the profile of the absorption line is underneath the chromospheric emission line. However, we measure our Mg II fluxes by simply integrating the fluxes of the emission line without trying to correct for any continuum that may be underneath the lines (see, e.g., Wood et al. 1996b, 2000a). This basically assumes that the photospheric absorption is broad and saturated underneath the line. This assumption will be a significant source of uncertainty ( $> 10\%$ ) only for the F stars in our sample, which have the strongest photospheric UV continua.

For those stars without high or moderate resolution HST spectra of Mg II, we look for high resolution IUE spectra that can be used to measure Mg II fluxes. Fluxes measured from IUE data are flagged in Table 3. In all our Mg II measurements we try to remove ISM absorption before making the flux measurements. This is difficult in high resolution IUE or moderate resolution HST spectra, since the narrow ISM lines are not well resolved. It is impossible in low resolution IUE spectra, which do not even have sufficient resolution to separate the two Mg II lines, so low resolution IUE spectra are not used here.

In order to convert measured fluxes to surface fluxes, we need to know the radii of our stars. Stellar radii are therefore listed in Table 3. We search the literature for radii that are measured via interferometry or by other direct means, and references in Table 3 indicate which radii come from such sources. However, we estimate most of our radii following the prescription of Wood et al. (1994), using the Barnes-Evans relation for most of the stars (Barnes, Evans, & Moffett 1978),



but the radius-luminosity relation of Grossman, Hays, & Graboske (1974) for the M dwarfs.

Finally, we wish to correlate our Ly $\alpha$  fluxes with rotation rates, so Table 3 also lists rotation periods found in the literature for our sample of stars. References in the table indicate the sources of the periods. Most are genuine photometric periods, but some are estimated from Ca II measurements and a known Ca II-rotation relation. The periods derived from Ca II are flagged in Table 3.

In Figures 15a-b, we plot Ly $\alpha$  surface fluxes versus X-ray and Mg II surface fluxes, and in Figure 15c the Ly $\alpha$  fluxes are plotted against rotation period. In addition to plotting the stellar data listed in Table 3, we also add a solar data point to these figures. We assume a solar Ly $\alpha$  flux of  $F_{Ly\alpha} = 3.5 \times 10^5$  ergs cm $^{-2}$  s $^{-1}$ , the midpoint of a range quoted by Woods et al. (2000). A figure in Woods et al. (2004) implies that quiescent solar Mg II k fluxes are about 1.6 times larger than Ly $\alpha$ . Given that the h line has about 75% the flux of the k line, we assume that the total Mg II h & k flux is 2.8 times that quoted above for Ly $\alpha$ ,  $F_{MgII} = 9.8 \times 10^5$  ergs cm $^{-2}$  s $^{-1}$ . Finally, the solar rotation period at the equator is about 26 days, and for the X-ray flux we assume a typical value of  $F_X = 3.25 \times 10^4$  ergs cm $^{-2}$  s $^{-1}$  for the Sun (Maggio et al. 1987).

The chromospheric Ly $\alpha$  fluxes are highly correlated with the chromospheric Mg II and coronal X-ray fluxes in Figures 15a-b, as expected. They are anti-correlated with rotation period in Figure 15c, consistent with many previous studies showing how rapid rotation induces higher degrees of chromospheric and coronal activity in cool stars (e.g., Mathioudakis et al. 1995). The Sun is nicely consistent with the other G star data points in Figures 15a-c, which is encouraging. Figures 15a-c show separate least squares fits to the F V+G V, K V, and giant (III) stars, in addition to fits to all the stars combined. We combine the F V stars with the G V stars since the few F V stars are all late F stars and these data points are basically consistent with the more numerous G stars. There are not enough subgiants (IV) and M V stars to justify making separate fits to those data. In order to estimate uncertainties in the fit parameters, we use a Monte Carlo method. For a large number of trials, we randomly vary the data points within assumed error bars, conduct new fits for each of these trials, and see how much the fit parameters vary.

The assumed error bars are estimated as follows. The biggest source of uncertainty in the fluxes is generally target variability rather than measurement uncertainty. Ayres (1997) estimates that *ROSAT* PSPC fluxes should cover a range of about a factor of 4 during solar-like activity cycles, so we assume 0.3 dex uncertainties for the  $F_X$  values. The solar Ly $\alpha$  flux range quoted by Woods et al. (2000) represents a  $\pm 20\%$  variation from the median value due to solar cycle and rotational variability. We assume this result roughly applies to the Mg II fluxes as well and therefore estimate 0.08 dex uncertainties for  $F_{MgII}$ . Combining this uncertainty with the previously quoted  $\approx 20\%$  measurement uncertainty for the Ly $\alpha$  fluxes leads us to assume 30% (0.11 dex) uncertainties for  $F_{Ly\alpha}$ . Probably the major source of uncertainty for the rotation periods is the presence of differential rotation, which leads to  $P_{rot}$  being a somewhat ill-defined parameter. We conservatively assume 20% (0.08 dex) errors for this quantity. Table 4 lists the resulting fit parameters and  $1\sigma$  uncertainties

for all the fits in Figures 15a-c.

Although Ly $\alpha$  and Mg II are both broadly called chromospheric lines, the relations between  $F_{Ly\alpha}$  and  $F_{MgII}$  in Figure 15b are not quite linear. For example, the power law index for the F V+G V stars quoted in Table 4 is  $0.82 \pm 0.04$ . This is well below 1 and suggests that the Ly $\alpha$  flux increases more rapidly with activity than Mg II. This effect is also evident when comparing our  $F_{Ly\alpha} - F_X$  relations with the  $F_{MgII} - F_X$  relations from Ayres et al. (1995). For solar-like G dwarfs, we find  $F_X \propto F_{Ly\alpha}^{2.20 \pm 0.13}$  while Ayres et al. (1995) quotes  $F_X \propto F_{MgII}^{2.85 \pm 0.17}$ . Since higher temperature lines are known to exhibit stronger increases when plotted as a function of any activity diagnostic, these results suggest that the Ly $\alpha$  line is formed at somewhat hotter temperatures than Mg II, consistent with the predictions of atmospheric models (Vernazza, Avrett, & Loeser 1981). It is interesting that the  $F_{Ly\alpha} - F_{MgII}$  relation of the giant stars appears to be noticeably more linear than for the dwarfs, and surprisingly tight considering the diverse makeup of this group of stars.

Guinan, Ribas, & Harper (2003) quote a power law index of  $-1.49$  in their plot of C II fluxes versus  $P_{rot}$  for a selection of solar-like G stars. This is somewhat steeper than our analogous  $F_{Ly\alpha} - P_{rot}$  relation, which has a power law of  $-1.09 \pm 0.08$  (see Table 4). This suggests that the Ly $\alpha$  lines are formed at temperatures cooler than C II, and therefore somewhere in between the Mg II and C II line formation temperatures.

The K dwarf relations in Figures 15a and 15c are reasonably tight, but this is not the case in 15b. The K star data points in Figure 15b show a lot of scatter, with the two largest discrepancies being the two latest type stars, 61 Cyg A and  $\epsilon$  Ind (both K5 V). Given that the two M dwarfs in the figure are also discrepant in the same sense, perhaps the relation between Mg II and Ly $\alpha$  undergoes a drastic change for stars with spectral types later than early K. It is also interesting to note that the K dwarf power law relation in Figure 15a is noticeably steeper than that of the G star relation, while in Figure 15c it is noticeably shallower. The implication is that for a given increase in rotation, the chromospheric and coronal emission from K stars increases less than that of G stars, but for a given increase in chromospheric emission the X-ray fluxes of K stars increase *more* than the G stars.

The last panel of Figure 15 compares our HST Ly $\alpha$  fluxes with previous measurements from IUE data. Analyzing the Ly $\alpha$  line in IUE spectra is much more difficult than in HST spectra for many reasons. The S/N is lower, the spectral resolution is poorer, and not only must one correct for ISM absorption but also for geocoronal contamination, which can be severe due to the much larger apertures of IUE compared with HST. Landsman & Simon (1993) developed techniques to deal with these difficulties and the IUE measurements plotted in Figure 15d are from their work. Despite the complications with the IUE analysis, the agreement between the IUE and HST fluxes is reasonably good. Some of the scatter could be due to real stellar variability. For the lower fluxes, the IUE measurements tend to be systematically higher than suggested by HST, which may be due to inaccuracies in the IUE's flux calibration at Ly $\alpha$  or due to the difficulties in subtracting

the geocoronal signal. The only data point in Figure 15d that is truly discrepant is EV Lac, which has an IUE flux about an order of magnitude larger than the HST flux. As this M dwarf is a well known flare star, perhaps there was a strong flare during the IUE observation.

## 8. SUMMARY

We have analyzed 33 HST/STIS E140M Ly $\alpha$  spectra of cool stars located within 100 pc, in order to measure chromospheric Ly $\alpha$  fluxes, determine line-of-sight interstellar H I and D I properties, and search for detections of heliospheric and astrospheric absorption. Our findings are summarized as follows.

1. We find that the geocoronal Ly $\alpha$  emission lines in our spectra tend to be blueshifted with respect to their expected locations by  $-1.20 \pm 0.90$  km s $^{-1}$ , indicating a systematic error in the wavelength calibration of STIS E140M spectra, at least in the Ly $\alpha$  wavelength region.
2. Our analysis of the D I and H I Ly $\alpha$  absorption lines has led to 4 new detections of heliospheric Ly $\alpha$  absorption (70 Oph,  $\xi$  Boo, 61 Vir, and HD 165185), bringing the total number of detections to 8. We find 7 new astrospheric detections (EV Lac, 70 Oph,  $\xi$  Boo, 61 Vir,  $\delta$  Eri, HD 128987, and DK UMa), although we consider the 61 Vir and DK UMa detections to be marginal. This brings the total number of detected astrospheres to 13.
3. We have measured interstellar H I column densities for all 33 lines of sight, which are listed in Tables 1 and 2. Of particular interest are the surprisingly high column densities towards AD Leo [ $\log N(\text{H I}) = 18.47$ ] and HD 203244 [ $\log N(\text{H I}) = 18.82$ ]. For the short 4.69 pc line of sight to AD Leo, the suggested average density of  $n(\text{H I}) = 0.204$  cm $^{-3}$  represents a new high for a Local Bubble line of sight. The rarity of  $\log N(\text{H I}) > 18.8$  lines of sight within the Local Bubble implies that detections of column densities this high are probably due to compact clouds that likely have densities well above the  $n(\text{H I}) \approx 0.1$  cm $^{-3}$  values believed to apply to the very local ISM within 10 pc.
4. When plotting ISM H I column densities versus  $\theta$ , the angle between the line of sight and the upwind direction of the ISM flow, the heliospheric detections are nicely separated from the nondetections. Only lines of sight with low ISM H I column densities have detected heliospheric absorption, and it is much easier to detect the heliospheric absorption in upwind directions (i.e.,  $\theta < 90^\circ$ ). In the most upwind directions, an ISM column of  $\log N(\text{H I}) < 18.2$  is required to detect heliospheric absorption, while in downwind directions one must have  $\log N(\text{H I}) < 17.8$ . This behavior is consistent with expectations from heliospheric models and represents further strong evidence in support of the heliospheric interpretation of the excess red-side Ly $\alpha$  absorption.
5. Within 10 pc, 10 of the 17 analyzed HST lines of sight have yielded detections of astrospheric absorption, for a detection rate of 58.8%. Since the presence of H I in the surrounding ISM is

one necessary ingredient for an astrospheric detection, the 58.8% detection fraction represents a lower limit for the filling factor of neutral ISM material within 10 pc, meaning that neutral hydrogen must be present in most of the ISM within 10 pc. However, beyond 10 pc only 3 of 31 HST lines of sight have astrospheric detections, for a much lower detection rate of 9.7%. Some of this difference is due to generally higher ISM H I column densities for longer lines of sight, which results in broader ISM absorption that can hide the astrospheric signal. However, beyond 10 pc most of the stars are probably surrounded by the hot, ionized ISM material that is believed to fill most of the Local Bubble, and this will account for many nondetections of astrospheric absorption beyond 10 pc.

6. Our Ly $\alpha$  absorption analyses requires the reconstruction of intrinsic stellar Ly $\alpha$  emission lines. We use these lines to measure chromospheric H I Ly $\alpha$  fluxes for our sample of stars, which are corrected for ISM absorption. We correlate these fluxes with coronal X-ray and chromospheric Mg II fluxes, and we also study the dependence of Ly $\alpha$  emission on rotation period. We present in Table 4 the derived relations for various classes of stars.

Support for this work was provided by grant AR-09957 from the Space Telescope Science Institute, which is operated by AURA, Inc., under NASA contract NAS5-26555.

## REFERENCES

- Ayres, T. R. 1997, *J. Geophys. Res.*, 102, 1641
- Ayres, T. R., et al. 1995, *ApJS*, 96, 223
- Baranov, V. B., & Malama, Y. G. 1993, *J. Geophys. Res.*, 98, 15157
- Baranov, V. B., & Malama, Y. G. 1995, *J. Geophys. Res.*, 100, 14755
- Barnes, S. A. 2001, *ApJ*, 561, 1095
- Barnes, T. G., Evans, D. S., & Moffett, T. J. 1978, *MNRAS*, 183, 285
- Benedict, G. F., et al. 1993, *PASP*, 105, 487
- Bertin, P., Vidal-Madjar, A., Lallement, R., Ferlet, R., & Lemoine, M. 1995, *A&A*, 302, 889
- Bevington, P. R., & Robinson, D. K. 1992, *Data Reduction and Error Analysis for the Physical Sciences* (New York: McGraw-Hill)
- Bond, H. E., Mullan, D. J., O'Brien, M. S., & Sion, E. M. 2001, *ApJ*, 560, 919
- Bordé, P., Coudé du Foresto, V., Chagnon, G., & Perrin, G. 2002, *A&A*, 393, 183
- Char, S., Foing, B. H., Beckman, J., Garcia-Lopez, R. J., & Rebolo, R. 1993, *A&A*, 276, 78
- Charbonneau, D., Brown, T. M., Latham, D. W., & Mayor, M. 2000, *ApJ*, 529, L45
- Choi, H. -J., Soon, W., Donahue, R. A., Baliunas, S. L., & Henry, G. W. 1995, *PASP*, 107, 744
- Cutispoto, G., Kürster, M., Pagano, I., & Rodonò, M. 1997, *IBVS*, No. 4419
- Cutispoto G., Pastori L., Tagliaferri G., Messina S., & Pallavicini R. 1999, *A&AS*, 138, 87
- Donahue, R. A., Saar, S. H., & Baliunas, S. L. 1996, *ApJ*, 466, 384
- Donnelly, R. F., White, O. R., & Livingston, W. C. 1994, *Sol. Phys.*, 152, 69
- Dring, A. R., Linsky, J., Murthy, J., Henry, R. C., Moos, W., Vidal-Madjar, A., Audouze, J., & Landsman, W. 1997, *ApJ*, 488, 760
- Fekel, F. C., Jr. 1983, *ApJ*, 268, 274
- Frick, P., Soon, W., Popova, E., & Baliunas, S. 2004, *New Astronomy*, 9, 599
- Frisch, P. C. 2003, *ApJ*, 593, 868
- Frisch, P. C. 1993, *ApJ*, 407, 198

- Frisch, P. C., Grodnicki, L., & Welty, D. E. 2002, *ApJ*, 574, 834
- Frisch, P. C., & Slavin, J. D. 2003, *ApJ*, 594, 844
- Gaidos, E. J., Henry, G. W., & Henry, S. M. 2000, *AJ*, 120, 1006
- Gayley, K. G., Zank, G. P., Pauls, H. L., Frisch, P. C., & Welty, D. E. 1997, *ApJ*, 487, 259
- Grossman, A. S., Hays, D., & Graboske, H. C., Jr. 1974, *A&A*, 30, 95
- Guinan, E. F., Ribas, I., & Harper, G. M. 2003, *ApJ*, 594, 561
- Hallam, K. L., Altner, B., & Endal, A. S. 1991, *ApJ*, 372, 610
- Hawley, S. L., et al. 2003, *ApJ*, 597, 535
- Hébrard, G., et al. 2002, *ApJS*, 140, 103
- Hempelmann, A., Schmitt, J. H. M. M., Schultz, M., Rüdiger, G., & Stepień, K. 1995, *A&A*, 294, 515
- Hooten, J. T., & Hall, D. S. 1990, *ApJS*, 74, 225
- Hummel, C. A., Armstrong, J. T., Quirrenbach, A., Buscher, D. F., Mozurkewich, D., Elias, N. M., II, & Wilson, R. E. 1994, *AJ*, 107, 1859
- Hünsch, M., Schmitt, J. H. M. M., & Voges, W. 1998a, *A&AS*, 127, 251
- Hünsch, M., Schmitt, J. H. M. M., & Voges, W. 1998b, *A&AS*, 132, 155
- Izmodenov, V. V., Geiss, J., Lallement, R., Gloeckler, G., Baranov, V. B., & Malama, Y. G. 1999a, *J. Geophys. Res.*, 104, 4731
- Izmodenov, V. V., Lallement, R., & Malama, Y. G. 1999b, *A&A*, 342, L13
- Jetsu, L. 1993, *A&A*, 276, 345
- Jetsu, L. 1996, *A&A*, 314, 153
- Kalas, P., Liu, M. C., & Matthews, B. C. 2004, *Science*, 303, 1990
- Kervella, P., Thévenin, F., Morel, P., Berthomieu, G., Bordé, P., & Provost, J. 2004, *A&A*, 413, 251
- Kervella, P., Thévenin, F., Ségransan, D., Berthomieu, G., Lopez, B., Morel, P., & Provost, J. 2003, *A&A*, 404, 1087
- Kruk, J. W., et al. 2002, *ApJS*, 140, 19
- Lallement, R., & Bertin, P. 1992, *A&A*, 266, 479

- Lallement, R., Ferlet, R., Lagrange, A. M., Lemoine, M., & Vidal-Madjar, A. 1995, *A&A*, 304, 461
- Lallement, R., Welsh, B. Y., Vergely, J. L., Crifo, F., & Sfeir, D. 2003, *A&A*, 411, 447
- Landsman, W., & Simon, T. 1993, *ApJ*, 408, 305
- Lehner, N., Gry, C., Sembach, K. R., Hébrard, G., Chayer, P., Moos, H. W., Howk, J. C., & Désert, J. -M. 2002, *ApJS*, 140, 81
- Lemaire, P., Emerich, C., Curdt, W., Schuehle, U., & Wilhelm, K. 1998, *A&A*, 334, 1095
- Lemoine, M., et al. 2002, *ApJS*, 140, 67
- Lindler, D. 1999, *CALSTIS Reference Guide (Greenbelt: NASA/LASP)*
- Linsky, J. L. 1998, *Space Sci. Rev.*, 84, 285
- Linsky, J. L., Diplas, A., Wood, B. E., Brown, A., Ayres, T. R., & Savage, B. D. 1995a, *ApJ*, 451, 335
- Linsky, J. L., Redfield, S., Wood, B. E., & Piskunov, N. 2000, *ApJ*, 528, 756
- Linsky, J. L., & Wood, B. E. 1996, *ApJ*, 463, 254
- Linsky, J. L., Wood, B. E., Brown, A., & Osten, R. A. 1998, *ApJ*, 492, 767
- Linsky, J. L., Wood, B. E., Judge, P., Brown, A., Andrulis, C., & Ayres, T. R. 1995b, *ApJ*, 442, 381
- Liu, M. C. 2004, *Science*, 305, 1442
- Maggio, A., et al. 1987, *ApJ*, 315, 687
- Mantegazza, L., Poretti, E., Antonello, E., & Bossi, M. 1992, *A&A*, 256, 459
- Mathioudakis, M., Fruscione, A., Drake, J. J., McDonald, K., Bowyer, S., & Malina, R. F. 1995, *A&A*, 300, 775
- Messina, S., Guinan, E. F., Lanza, A. F., & Ambruster, C. 1999, *A&A*, 347, 249
- Moos, H. W., et al. 2002, *ApJS*, 140, 3
- Morton, D. C. 2003, *ApJS*, 149, 205
- Mozurkewich, D., et al. 2003, *AJ*, 126, 2502
- Mullan, D. J., Sion, E. M., Bruhweiler, F. C., & Carpenter, K. G. 1989, *ApJ*, 339, L33
- Nelson, B., & Young, A. 1970, *PASP*, 82, 699

- Nordgren, T. E., et al. 1999, *AJ*, 118, 3032
- Noyes, R. W., Hartmann, L. W., Baliunas, S. L., Duncan, D. K., & Vaughan, A. H. 1984, *ApJ*, 279, 763
- O’Brien, M. S., Bond, H. E., & Sion, E. M. 2001, *ApJ*, 563, 971
- Oliveira, C. M., Hébrard, G., Howk, J. C., Kruk, J. W., Chayer, P., & Moos, H. W. 2003, *ApJ*, 587, 235
- Opher, M., Liewer, P. C., Gombosi, T. I., Manchester, W., DeZeeuw, D. L., Sokolov, I., & Toth, G. 2003, *ApJ*, 591, L61
- Pauls, H. L. and Zank, G. P. 1997, *J. Geophys. Res.*, 102, 19,779
- Paulson, D. B., Cochran, W. D., & Hatzes, A. P. 2004, *AJ*, 127, 3579
- Pijpers, F. P., Teixeira, T. C., Garcia, P. J., Cunha, M. S., Monteiro, M. J. P. F. G., & Christensen-Dalsgaard, J. 2003, *A&A*, 406, L15
- Piskunov, N., Wood, B. E., Linsky, J. L., Dempsey, R. C., & Ayres, T. R. 1997, *ApJ*, 474, 315
- Quémerais, E., Bertaux, J. -L., Sandel, B. R., & Lallement, R. 1994, *A&A*, 290, 941
- Ratkiewicz, R., Barnes, A., Molvik, G. A., Spreiter, J. R., Stahara, S. S., Vinokur, M., & Venkateswaran, S. 1998, *A&A*, 335, 363
- Redfield, S., & Linsky, J. L. 2000, *ApJ*, 534, 825
- Redfield, S., & Linsky, J. L. 2002, *ApJS*, 139, 439 (RL02)
- Redfield, S., & Linsky, J. L. 2004a, *ApJ*, 602, 776
- Redfield, S., & Linsky, J. L. 2004b, *ApJ*, 613, 1004
- Saar, S. H., & Osten, R. A. 1997, *MNRAS*, 284, 803
- Sahu, K. C., et al. 1999, *STIS Instrument Handbook* (Baltimore: STScI)
- Schmitt, J. H. M. M., & Liefke, C. 2004, *A&A*, 417, 651
- Ségransan, D., Kervella, P., Forveille, T., & Queloz, D. 2003, *A&A*, 397, L5
- Sfeir, D. M., Lallement, R., Crifo, F., & Welsh, B. Y. 1999, *A&A*, 346, 785
- Slavin, J. D., & Frisch, P. C. 2002, *ApJ*, 565, 364
- Stern, R. A., Schmitt, J. H. M. M., & Kahabka, P. T. 1995, *ApJ*, 448, 683
- Strassmeier, K. G., Reegen, P., & Granzer, T. 2001, *Astronomische Nachrichten*, 322, 115



- Strassmeier, K. G., Serkowitsch, P., & Granzer, T. 1999, *A&AS*, 140, 29
- Vennes, S., Polomski, E. F., Lanz, T., Thorstensen, J. R., Chayer, P., & Gull, T. R. 2000, *ApJ*, 544, 423
- Vernazza, J. E., Avrett, E. H., & Loeser, R. 1981, *ApJS*, 45, 635
- Vidal-Madjar, A., et al. 1998, *A&A*, 338, 694
- Vidal-Madjar, A., & Ferlet, R. 2002, *ApJ*, 571, L169
- Vidal-Madjar, A., Lecavelier des Etangs, A., Désert, J. -M., Ballester, G. E., Ferlet, R., Hébrard, G., & Mayor, M. 2003, *Nature*, 422, 143
- Vilhu, O., & Rucinski, S. M. 1983, *A&A*, 127, 5
- Witte, M. 2004, *A&A*, 426, 835
- Witte, M., Rosenbauer, H., Banaszekwicz, M., & Fahr, H. 1993, *Adv. Space Res.*, 13, 121
- Wood, B. E. 2004, *Living Rev. Solar Phys.*, 1, 2, URL: <http://www.livingreviews.org/lrsp-2004-2>
- Wood, B. E., Alexander, W. R., & Linsky, J. L. 1996a, *ApJ*, 470, 1157
- Wood, B. E., Ambruster, C. W., Brown, A., & Linsky, J. L. 2000a, *ApJ*, 542, 411
- Wood, B. E., Brown, A., Linsky, J. L., Kellett, B. J., Bromage, G. E., Hodgkin, S. T., & Pye, J. P. 1994, *ApJS*, 93, 287
- Wood, B. E., Harper, G. M., Linsky, J. L., & Dempsey, R. C. 1996b, *ApJ*, 458, 761
- Wood, B. E., & Linsky, J. L. 1998, *ApJ*, 492, 788
- Wood, B. E., Linsky, J. L., Hébrard, G., Vidal-Madjar, A., Lemoine, M., Moos, H. W., Sembach, K. R., & Jenkins, E. B. 2002a, *ApJS*, 140, 91
- Wood, B. E., Linsky, J.L., Hébrard, G., Williger, G. M., Moos, H. W., & Blair, W. P. 2004, *ApJ*, 609, 838
- Wood, B. E., Linsky, J. L., Müller, H. -R., & Zank, G. P. 2001, *ApJ*, 547, L49
- Wood, B. E., Linsky, J. L., & Zank, G. P. 2000b, *ApJ*, 537, 304
- Wood, B. E., Müller, H. -R., & Zank, G. P. 2000c, *ApJ*, 542, 493
- Wood, B. E., Müller, H. -R., Zank, G. P., & Linsky, J. L. 2002b, *ApJ*, 574, 412
- Woods, T. N., et al. 2004, *Geophys. Res. Lett.*, 31, L10802
- Woods, T. N., Tobiska, W. K., Rottman, G. J., & Worden, J. R. 2000, *J. Geophys. Res.*, 105, 27195

York, D. G., & Rogerson, J. B. 1976, ApJ, 203, 378

Young, A., Ajir, F., & Thurman, G. 1989, PASP, 101, 1017

Zank, G. P., Pauls, H. L., Williams, L. L., & Hall, D. T. 1996, J. Geophys. Res., 101, 21639

Table 1. Line of Sight Information for HST Ly $\alpha$  Targets

ID #	HD #	Other Name	Spectral Type	Dist. (pc)	l (deg)	b (deg)	log $N(\text{H I})$	Mg II?	Hel. Det.?	Ast. Det.?	Ref.
PREVIOUS ANALYSES											
1		Proxima Cen	M5.5 V	1.30	313.9	-1.9	17.61	No	Yes	No	1
2	128620	$\alpha$ Cen A	G2 V	1.35	315.7	-0.7	17.61	Yes	Yes	Yes	2
3	128621	$\alpha$ Cen B	K0 V	1.35	315.7	-0.7	17.61	Yes	Yes	Yes	2
4	48915	Sirius	A1 V	2.64	227.2	-8.9	17.53	Yes	Yes	...	3
5	22049	$\epsilon$ Eri	K1 V	3.22	195.8	-48.1	17.88	Yes	No	Yes	4
6	201091	61 Cyg A	K5 V	3.48	82.3	-5.8	18.13	Yes	No	Yes	5
7	61421	Procyon	F5 IV-V	3.50	213.7	13.0	18.06	Yes	...	...	6
8	209100	$\epsilon$ Ind	K5 V	3.63	336.2	-48.0	18.00	No	No	Yes	7
9	26965	40 Eri A	K1 V	5.04	200.8	-38.1	17.85	Yes	No	No	5
10	155886	36 Oph A	K1 V	5.99	358.3	6.9	17.85	Yes	Yes	Yes	8
11	62509	$\beta$ Gem	K0 III	10.3	192.2	23.4	18.26	Yes	No	No	4
12	17925	EP Eri	K2 V	10.4	192.1	-58.3	18.05	No	...	...	9
13	34029	Capella	G8 III+G1 III	12.9	162.6	4.6	18.24	Yes	No	No	6
14	432	$\beta$ Cas	F2 IV	16.7	117.5	-3.3	18.13	Yes	No	No	4
15	82443	DX Leo	K0 V	17.7	201.2	46.1	17.70	No	...	...	9
16	82558	LQ Hya	K2 V	18.3	244.6	28.4	19.05	No	...	...	9
17	11443	$\alpha$ Tri	F6 IV	19.7	138.6	-31.4	18.33	Yes	No	No	4
18	220140	V368 Cep	K2 V	19.7	118.5	16.9	17.95	No	...	...	9
19	1405	PW And	K2 V	21.9	114.6	-31.4	18.35	No	...	...	9
20	222107	$\lambda$ And	G8 IV-III+M V	25.8	109.9	-14.5	18.45	No	No	Yes?	7
21	22468	HR 1099	K1 IV+G5 IV	29.0	184.9	-41.6	18.13	Yes	No	No	10
22	4128	$\beta$ Cet	K0 III	29.4	111.3	-80.7	18.36	Yes	...	...	10
23		HZ 43	DA	32.0	54.1	84.2	17.93	Yes	Yes?	...	11
24	62044	$\sigma$ Gem	K1 III	37.5	191.2	23.3	18.20	Yes	No	No	4
25	197890	Speedy Mic	K2-3 V	44.4	6.3	-38.3	18.30	No	...	...	9
26		G191-B2B	DA	68.8	156.0	7.1	18.18	Yes	No	...	12
27		Feige 24	DA	74.4	166.0	-50.3	18.47	No	No	...	13
28		GD 246	DA	79.0	87.3	-45.1	19.11	No	No	...	14
29	111812	31 Com	G0 III	94.2	115.0	89.6	17.88	Yes	No	No	4
NEW ANALYSES <sup>a</sup>											
30	10700	$\tau$ Cet	G8 V	3.65	173.1	-73.4	18.01	No	No	No	15
31		AD Leo	M3.5 V	4.69	216.5	54.6	18.47	No	No	No	15
32		EV Lac	M3.5 V	5.05	100.6	-13.1	17.97	No	No	Yes	15
33	165341	70 Oph A	K0 V	5.09	29.9	11.4	18.06	Yes	Yes	Yes	15
34	131156A	$\xi$ Boo A	G8 V	6.70	23.1	61.4	17.92	Yes	Yes	Yes	15
35	115617	61 Vir	G5 V	8.53	311.9	44.1	17.91	No	Yes	Yes?	15
36	39587	$\chi^1$ Ori	G0 V	8.66	188.5	-2.7	17.93	Yes	No	No	15
37	23249	$\delta$ Eri	K0 IV	9.04	198.1	-46.0	17.88	No	No	Yes	15
38	20630	$\kappa$ Cet	G5 V	9.16	178.2	-43.1	17.89	Yes	No	No	15
39	197481	AU Mic	M0 V	9.94	12.7	-36.8	18.36	Yes	No	No	15
40	33262	$\zeta$ Dor	F7 V	11.7	266.0	-36.7	18.29	Yes	No	No	15
41	37394	HR 1925	K1 V	12.2	158.4	12.0	18.26	No	No	No	15
42	166	HR 8	K0 V	13.7	111.3	-32.8	18.29	No	No	No	15
43	142373	$\chi$ Her	F8 V	15.9	67.7	50.3	18.25	No	No	No	15

Table 1—Continued

ID #	HD #	Other Name	Spectral Type	Dist. (pc)	l (deg)	b (deg)	log $N(\text{H I})$	Mg II?	Hel. Det.?	Ast. Det.?	Ref.
44	43162	HR 2225	G5 V	16.7	230.9	-18.5	17.87	No	No	No	15
45	165185	HR 6748	G5 V	17.4	356.0	-7.3	18.13	No	Yes	No	15
46	203244	SAO 254993	G5 V	20.5	324.9	-38.9	18.82	No	No	No	15
47	97334	HR 4345	G0 V	21.7	184.3	67.3	17.82	No	No	No	15
48	59967	HR 2882	G4 V	21.8	250.5	-9.0	18.54	No	No	No	15
49	116956	SAO 28753	G9 IV-V	21.9	113.7	59.5	18.19	No	No	No	15
50	106516	HR 4657	F5 V	22.6	288.5	51.5	18.57	No	No	No	15
51	73350	SAO 136111	G0 V	23.6	232.1	20.0	18.16	No	No	No	15
52	128987	SAO 158720	G6 V	23.6	337.5	39.2	18.11	No	No	Yes	15
53	82210	DK UMa	G4 III-IV	32.4	142.6	38.9	18.05	Yes	No	Yes?	15
54	93497	$\mu$ Vel	G5 III	35.3	283.0	8.6	18.47	No	No	No	15
55	28568	SAO 93981	F2 V	41.2	180.5	-21.4	18.12	Yes	No	No	15
56	28205	V993 Tau	G0 V	45.8	180.4	-22.4	18.11	Yes	No	No	15
57	28033	SAO 76609	F8 V	46.4	175.4	-18.9	18.15	Yes	No	No	15
58		V471 Tau	K0 V	46.8	172.5	-27.9	18.21	No	No	No	15
59	209458	V376 Peg	G0 V	47.1	76.8	-28.5	18.37	No	No	No	15
60	220657	$\nu$ Peg	F8 III	53.1	98.6	-35.4	18.24	Yes	No	No	15
61	32008	HR 1608	G7 IV-III	54.7	209.6	-29.4	18.08	No	No	No	15
62	203387	$\iota$ Cap	G8 III	66.1	33.6	-40.8	18.70	Yes	No	No	15

<sup>a</sup>All new analyses are from HST/STIS E140M spectra, with a resolution of  $R \approx 45,000$ .

References. — (1) Wood et al. 2001. (2) Linsky & Wood 1996. (3) Bertin et al. 1995. (4) Dring et al. 1997. (5) Wood & Linsky 1998. (6) Linsky et al. 1995a. (7) Wood et al. 1996a. (8) Wood et al. 2000b. (9) Wood et al. 2000a. (10) Piskunov et al. 1997. (11) Kruk et al. 2002. (12) Lemoine et al. 2002. (13) Vennes et al. 2000. (14) Oliveira et al. 2003. (15) This paper.

Table 2. Ly $\alpha$  Fit Parameters

ID #	$V_{LIC}$ (km s $^{-1}$ )	$V_G$ (km s $^{-1}$ )	Comp. <sup>a</sup>	$v(\text{Mg II})^b$ (km s $^{-1}$ )	$v(\text{H I})^c$ (km s $^{-1}$ )	$b(\text{H I})^c$ (km s $^{-1}$ )	$\log N(\text{H I})^c$	$\chi^2_\nu$	Notes <sup>d</sup>
30	13.8	17.6	1	...	12.34 $\pm$ 0.06	10.32 $\pm$ 0.06	18.006 $\pm$ 0.002	1.106	
31	6.4	5.2	1	...	13.13 $\pm$ 0.05	14.05 $\pm$ 0.06	18.475 $\pm$ 0.001	2.571	*
32	3.5	5.2	1	...	7.3 $\pm$ 0.3	11.1 $\pm$ 0.2	17.972 $\pm$ 0.007	0.820	*
			HS/AS	...	-6.7 $\pm$ 2.2	29.1 $\pm$ 1.2	14.46 $\pm$ 0.07		
33	-23.5	-26.4	1	-26.64	-26.9 $\pm$ 0.2	8.7 $\pm$ 0.4	17.934 $\pm$ 0.003	0.851	*
			2	-32.91	-33.22	8.72	17.293		
			3	-43.36	-43.68	8.72	16.972		
			HS/AS	...	-32.62 $\pm$ 0.09	26.4 $\pm$ 0.5	15.39 $\pm$ 0.06		
34	-17.7	-21.6	1	-17.15	-19.3 $\pm$ 0.3	9.7 $\pm$ 0.6	17.915 $\pm$ 0.007	1.191	*
			HS/AS	...	-16.9 $\pm$ 0.3	19.2 $\pm$ 0.7	15.7 $\pm$ 0.1		
35	-15.4	-19.2	1	...	-16.5 $\pm$ 0.7	7.4 $\pm$ 1.5	17.91 $\pm$ 0.04	0.992	*
			HS/AS	...	-12.4 $\pm$ 0.9	18.1 $\pm$ 1.9	16.1 $\pm$ 0.5		
36	24.9	27.9	1	23.35	23.3 $\pm$ 0.1	11.95 $\pm$ 0.06	17.934 $\pm$ 0.003	1.251	
37	22.0	26.0	1	...	19.6 $\pm$ 0.2	11.8 $\pm$ 0.1	17.880 $\pm$ 0.007	1.061	*
			HS/AS	...	2.6 $\pm$ 0.9	31.3 $\pm$ 0.7	14.56 $\pm$ 0.03		
38	22.8	27.0	1	20.78	20.0 $\pm$ 0.4	11.1 $\pm$ 0.2	17.592 $\pm$ 0.006	0.967	*
			2	13.33	12.51	11.07	17.550		
			3	7.25	6.43	13.3 $\pm$ 0.2	16.545		
39	-15.3	-15.7	1	-21.22	-20.83 $\pm$ 0.09	13.74 $\pm$ 0.08	18.356 $\pm$ 0.002	0.879	*
40	7.8	9.4	2	8.45	8.6 $\pm$ 0.1	9.8 $\pm$ 0.5	18.090 $\pm$ 0.003	1.273	*
			1	14.12	14.27	14.8 $\pm$ 0.1	17.870		
41	19.8	22.1	1	...	17.5 $\pm$ 0.2	11.9 $\pm$ 0.3	18.256 $\pm$ 0.005	0.791	
42	9.4	12.3	1	...	6.5 $\pm$ 0.2	12.7 $\pm$ 0.2	18.290 $\pm$ 0.006	0.577	
43	-13.1	-15.9	1	...	-12.9 $\pm$ 0.1	12.4 $\pm$ 0.2	18.249 $\pm$ 0.003	0.920	
44	18.9	21.3	1	...	14.0 $\pm$ 0.2	12.8 $\pm$ 0.1	17.87 $\pm$ 0.01	1.106	
45	-23.2	-25.7	1	...	-29.2 $\pm$ 0.7	13.4 $\pm$ 0.9	18.13 $\pm$ 0.02	0.938	*
			HS/AS	...	-20.8 $\pm$ 3.5	17.8 $\pm$ 1.8	16.2 $\pm$ 0.5		
46	-9.9	-10.0	1	...	-13.1 $\pm$ 0.7	15.9 $\pm$ 1.2	18.82 $\pm$ 0.01	1.125	*
47	2.8	1.1	1	...	4.3 $\pm$ 0.2	11.7 $\pm$ 0.1	17.82 $\pm$ 0.01	1.022	
48	11.7	12.7	1	...	8.4 $\pm$ 0.4	14.0 $\pm$ 0.6	18.536 $\pm$ 0.008	1.095	
49	-2.5	-4.3	1	...	3.2 $\pm$ 0.3	13.8 $\pm$ 0.2	18.188 $\pm$ 0.009	1.499	
50	-9.0	-12.2	1	...	-3.4 $\pm$ 1.1	18.9 $\pm$ 0.8	18.57 $\pm$ 0.02	0.991	*
51	13.6	13.9	1	...	12.0 $\pm$ 0.4	12.8 $\pm$ 0.3	18.163 $\pm$ 0.009	1.224	
52	-21.4	-25.5	1	...	-22.0 $\pm$ 0.7	13.1 $\pm$ 0.4	18.11 $\pm$ 0.02	1.246	*
			HS/AS	...	-42.74	34.1 $\pm$ 2.4	14.39 $\pm$ 0.06		
53	9.3	9.5	1	9.63	8.30 $\pm$ 0.08	10.1 $\pm$ 0.3	18.051 $\pm$ 0.002	1.059	*
			HS/AS	...	5.4 $\pm$ 0.9	19.6 $\pm$ 0.8	15.2 $\pm$ 0.2		
54	-4.0	-5.6	1	...	-4.38 $\pm$ 0.05	12.90 $\pm$ 0.09	18.469 $\pm$ 0.001	1.607	
55	25.5	29.3	1	23.9	26.6 $\pm$ 0.6	12.4 $\pm$ 0.5	18.03 $\pm$ 0.02	0.887	
			2	16.5	19.21	12.42	17.371		
56	25.9	29.3	1	23.3	24.1 $\pm$ 0.6	12.7 $\pm$ 0.3	18.00 $\pm$ 0.01	0.920	
			2	14.8	15.65	12.74	17.471		
57	25.3	29.1	1	23.6	23.8 $\pm$ 0.8	12.8 $\pm$ 0.6	18.15 $\pm$ 0.02	0.860	
58	24.6	28.6	1	...	20.9 $\pm$ 0.3	12.3 $\pm$ 0.4	18.206 $\pm$ 0.007	0.948	*
59	-3.7	-2.5	1	...	-6.6 $\pm$ 0.9	12.3 $\pm$ 1.3	18.37 $\pm$ 0.02	0.949	*

Table 2—Continued

ID #	$V_{LIC}$ (km s <sup>-1</sup> )	$V_G$ (km s <sup>-1</sup> )	Comp. <sup>a</sup>	$v(\text{Mg II})^b$ (km s <sup>-1</sup> )	$v(\text{H I})^c$ (km s <sup>-1</sup> )	$b(\text{H I})^c$ (km s <sup>-1</sup> )	$\log N(\text{H I})^c$	$\chi^2_\nu$	Notes <sup>d</sup>
60	5.1	7.5	2	1.13 <sup>e</sup>	2.21 ± 0.09	11.62 ± 0.05	18.157 ± 0.001	1.076	*
			1	7.00 <sup>e</sup>	8.09	14.0 ± 1.4	17.157		
			3	-7.61 <sup>e</sup>	-6.52	13.4 ± 0.2	17.167		
61	23.3	26.8	1	...	6.1 ± 1.0	12.9 ± 0.3	17.69 ± 0.06	0.765	*
			2	...	21.6 ± 0.9	12.87	17.84 ± 0.05		
62	-11.8	-11.5	3	-2.17 <sup>e</sup>	-8.5 ± 0.1	15.9 ± 0.2	18.563 ± 0.002	1.681	*
			2	-12.67 <sup>e</sup>	-18.94	15.91	17.903		
			1	-19.35 <sup>e</sup>	-25.63	15.91	17.723		

<sup>a</sup>Component number, where we assign the same numbers as Redfield & Linsky (2002) when a correspondence exists. “HS/AS” indicates an absorption component that accounts for heliospheric and/or astrospheric absorption. It has been demonstrated previously that hydrodynamic modeling of the HS/AS absorption is required to truly quantify it properly, so the empirical fit parameters quoted here for the HS/AS components should be regarded with skepticism.

<sup>b</sup>ISM Mg II absorption velocity from Redfield & Linsky (2002).

<sup>c</sup>Quoted uncertainties are 1 $\sigma$  random errors in the fit, which do not include estimates of systematic errors (see §4.2).

<sup>d</sup>When indicated, see §4.5 for more information on the Ly $\alpha$  analysis.

<sup>e</sup>This is an Fe II velocity instead of Mg II.

Table 3. Stellar Information for HST Ly $\alpha$  Targets

ID #	Radius		$P_{rot}$		Fluxes ( $10^{-12}$ )		
	( $R_{\odot}$ )	Ref.	(days)	Ref.	Ly $\alpha$	Mg II	X-ray
1	0.15	1	41.6	11	4.21	...	8.21
2	1.22	2	29	12	101	398	10.7
3	0.86	2	43	13	150	285	12.1
5	0.78	...	11.7	14	48.8	61.7	16.8
6	0.68	...	35.4	14	17.2	14.2	1.94
7	2.05	3	...	...	148	512	22.1
8	0.75	...	22 <sup>a</sup>	15	31.0	15.1 <sup>b</sup>	1.56
9	0.82	...	42	16	6.93	11.6	1.09
10	0.69	...	20.7	14	14.2	11.0	2.93
11	8.83	4	...	...	42.3	98.5	0.36
12	0.93	...	6.76	14	6.05	13.4	7.21
13A	12.2	5	106	17	157	414	77.8
13B	9.2	5	8.64	17	268	683	63.2
14	3.80	6	...	...	21.7	...	0.97
15	0.80	...	5.38	18	2.31	5.87	4.43
16	0.73	...	1.60	19	4.01	5.10	16.5
17	3.04	...	1.74	20	38.8	115	6.07
18	0.80	...	2.77	21	2.99	5.52	17.5
19	0.68	...	1.75	22	2.31	2.54	9.14
20	7.4	6	54	23	75.3	171 <sup>b</sup>	82.9
21A	3.9	7	2.84	7	94.2	51.0	150
21B	1.3	7	2.84	7	7.57	4.1	...
22	16.8	8	...	...	85.1	158	26.6
24	9.3	6	19.6	24	74.0	107	74.8
25	0.85	...	0.38	25	1.85	1.64	36.7
29	8.9	...	6.96	24	11.1	35.4	11.6
30	0.77	9	34.5 <sup>a</sup>	15	9.99	14.0 <sup>b</sup>	0.31
31	0.38	...	2.6	26	9.95	2.79 <sup>b</sup>	24.0
32	0.35	...	4.38	26	2.75	...	32.0
33	0.85	...	19.7	27	21.4	27.8	6.01
34	0.78	...	6.31	14	18.5	32.4	14.8
35	1.00	...	...	...	1.69	4.53	0.085
36	0.98	...	5.36	14	12.7	25.0	11.7
37	2.58	...	55.3 <sup>a</sup>	27	7.82	16.3 <sup>b</sup>	0.11
38	0.99	...	9.24	14	8.44	14.9	7.21
39	0.61	...	4.85	26	10.3	4.20	36.1
40	0.96	...	...	...	7.99	18.5	2.86
41	0.88	...	10.9	28	4.57	7.02	2.24
42	0.90	...	6.23	28	4.77	7.17 <sup>b</sup>	4.15
43	1.56	...	16.8 <sup>a</sup>	27	2.04	4.20 <sup>b</sup>	0.029
44	0.87	...	...	...	3.45	...	4.04
45	0.94	...	5.9 <sup>a</sup>	15	3.73	7.71	4.08
46	0.89	...	...	...	2.47	3.33	1.14
47	1.01	...	8.25	28	2.09	5.29	1.95
48	0.89	...	...	...	2.76	4.45	2.07

Table 3—Continued

ID #	Radius		$P_{rot}$		Fluxes ( $10^{-12}$ )		
	( $R_{\odot}$ )	Ref.	(days)	Ref.	Ly $\alpha$	Mg II	X-ray
49	0.91	...	7.8	28	1.62	2.82	1.21
50	0.96	...	6.91	14	1.28	2.88	0.25
51	1.07	...	6.14	28	1.34	2.69	0.79
52	0.84	...	9.35	28	1.44	2.52	0.60
53	4.4	...	10 <sup>a</sup>	29	15.6	33.1	18.2
54	14.4	...	...	...	55.3	131 <sup>b</sup>	22.2
55	1.35	...	...	...	1.41	2.98	1.32
56	1.16	...	4.65	30	0.59	1.49	0.44
57	1.20	...	...	...	0.27	0.55	0.21
58	0.96	10	0.52	31	2.87	...	...
59	1.10	...	15.7 <sup>a</sup>	32	0.15	...	...
60	6.3	...	...	...	11.8	33.4	6.95
61	5.17	...	...	...	5.03	...	...
62	12.3	...	68	33	12.9	27.1	8.54

<sup>a</sup>Estimated from a Ca II-rotation relation rather than from a photometric periodicity.

<sup>b</sup>Measured from high resolution IUE spectra instead of HST data.

References. — (1) Ségransan et al. 2003. (2) Kervella et al. 2003. (3) Kervella et al. 2004. (4) Mozurkewich et al. 2003. (5) Hummel et al. 1994. (6) Nordgren et al. 1999. (7) Fekel 1983. (8) Bordé et al. 2002. (9) Pijpers et al. 2003. (10) O’Brien et al. 2001. (11) Benedict et al. 1993. (12) Hallam et al. 1991. (13) Char et al. 1993. (14) Donahue et al. 1996. (15) Saar & Osten 1997. (16) Frick et al. 2004. (17) Strassmeier et al. 2001. (18) Messina et al. 1999. (19) Jetsu 1993. (20) Vilhu & Rucinski 1983. (21) Mantegazza et al. 1992. (22) Hooten & Hall 1990. (23) Jetsu 1996. (24) Strassmeier et al. 1999. (25) Cutispoto et al. 1997. (26) Hempelmann et al. 1995. (27) Noyes et al. 1984. (28) Gaidos et al. 2000. (29) Young et al. 1989. (30) Paulson et al. 2004. (31) Nelson & Young 1970. (32) Barnes 2001. (33) Choi et al. 1995.



Table 4. Parameters for Fits in Figure 15

Equation	Spect. Type	$\alpha$	$\beta$
$\log F_X = \alpha \log F_{Ly\alpha} + \beta$	G V+F V	$2.20 \pm 0.13$	$-7.76 \pm 0.82$
	K V	$2.90 \pm 0.20$	$-12.11 \pm 1.28$
	III	$2.23 \pm 0.18$	$-7.70 \pm 1.06$
	all	$2.22 \pm 0.08$	$-7.81 \pm 0.47$
$\log F_{MgII} = \alpha \log F_{Ly\alpha} + \beta$	G V+F V	$0.82 \pm 0.04$	$1.43 \pm 0.26$
	K V	$0.89 \pm 0.06$	$0.82 \pm 0.40$
	III	$0.98 \pm 0.06$	$0.50 \pm 0.36$
	all	$0.71 \pm 0.02$	$2.04 \pm 0.14$
$\log F_{Ly\alpha} = \alpha \log P_{rot} + \beta$	G V+F V	$-1.09 \pm 0.08$	$7.14 \pm 0.08$
	K V	$-0.57 \pm 0.03$	$6.82 \pm 0.03$
	III	$-0.43 \pm 0.06$	$6.68 \pm 0.09$
	all	$-0.65 \pm 0.02$	$6.82 \pm 0.02$

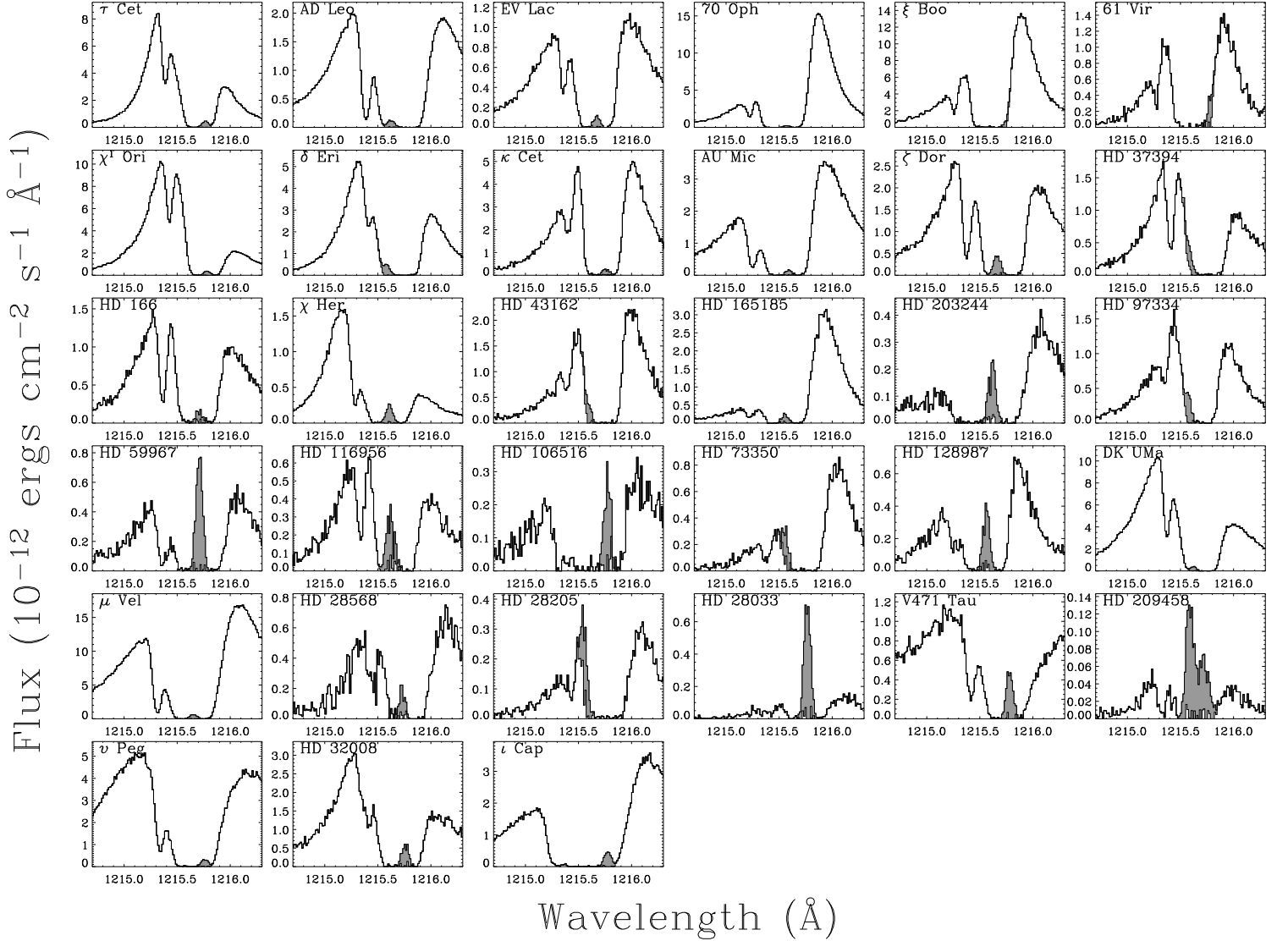


Fig. 1.— Spectra of the H I Ly $\alpha$  line. The observations are all HST/STIS E140M spectra. The spectra show very broad, saturated H I absorption from the ISM near line center, and most show weaker and narrower D I absorption  $-0.33$   $\text{\AA}$  from the center of the H I line. The shaded regions are geocoronal Ly $\alpha$  emission, which are subtracted from the spectra before the H I and D I absorption lines are analyzed.

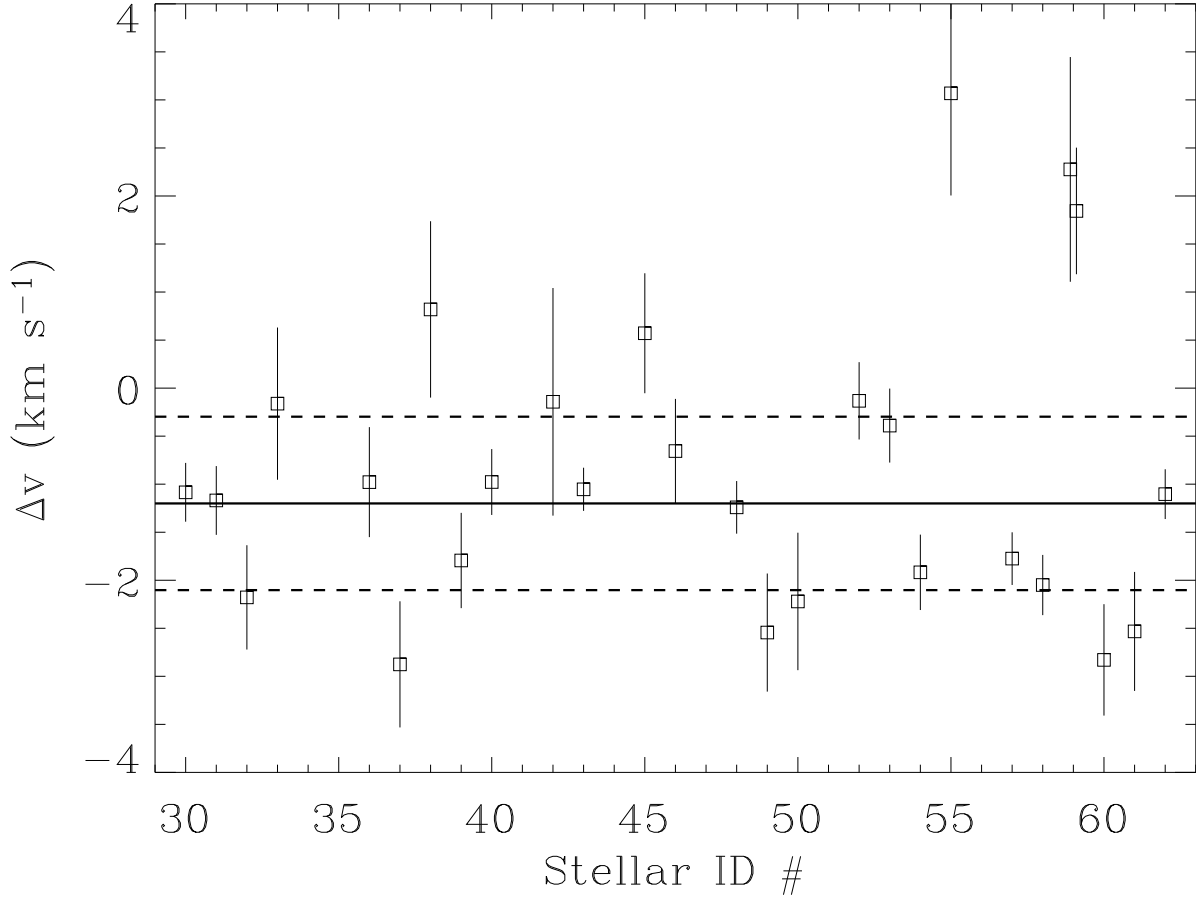


Fig. 2.— We subtract from the measured centroid of the geocoronal Ly $\alpha$  emission line its expected velocity (i.e.,  $\Delta v \equiv v_{\text{obs}} - v_{\text{geo}}$ ) and plot the resulting velocity discrepancies for all the newly analyzed spectra shown in Fig. 1, where the stellar ID numbers refer to those used in Table 1. We cannot measure a centroid in cases where the geocoronal emission is blended with the stellar emission, so no point is plotted for some stars. For star #59 there are two points plotted since there are observations at two different times. The horizontal solid line and the dashed lines show the weighted mean and standard deviation of the  $\Delta v$  values,  $\Delta v = -1.20 \pm 0.90$  km s<sup>-1</sup>.

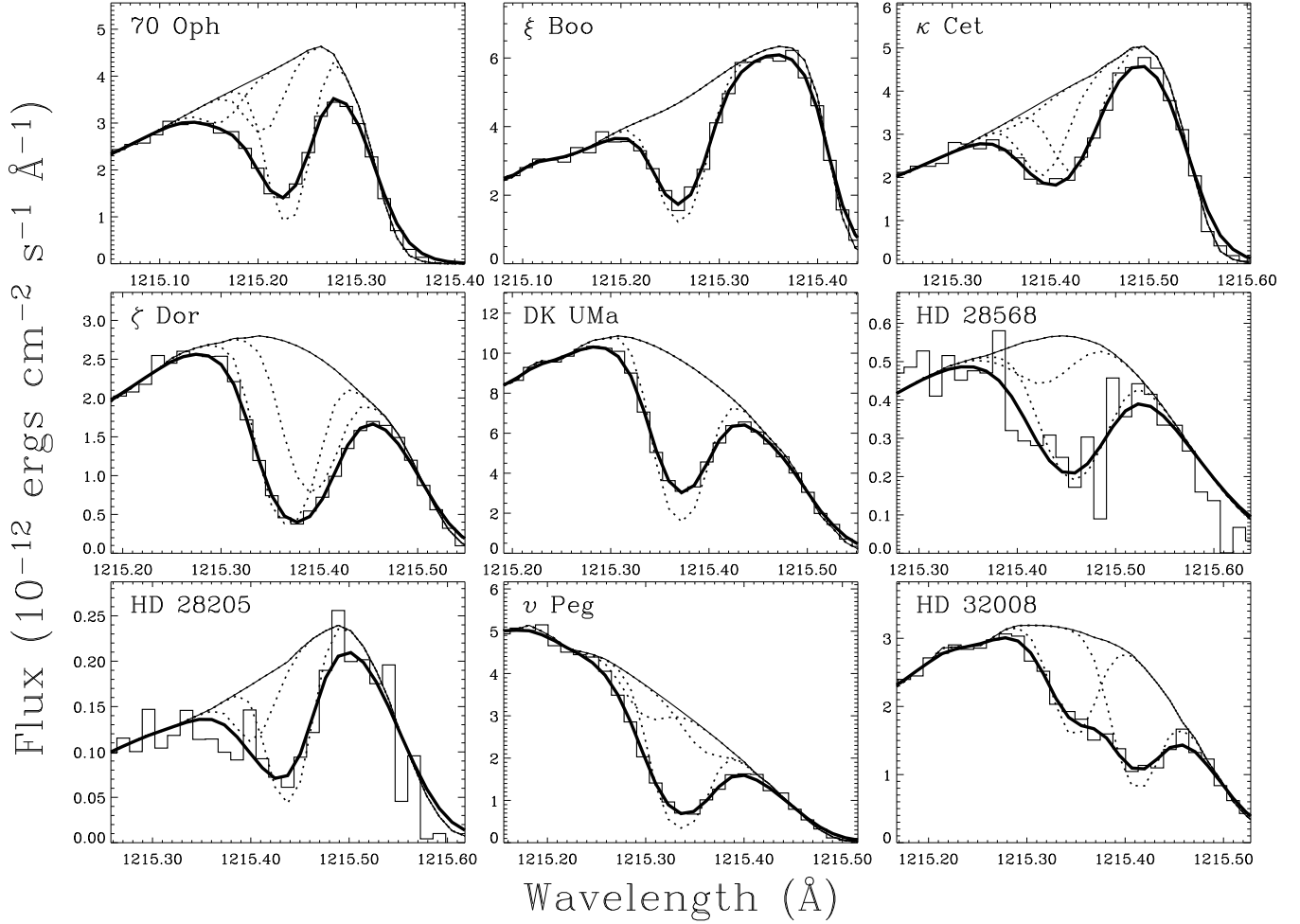


Fig. 3.— Fits to the D I Ly $\alpha$  absorption line for selected stars. Dotted lines show the individual components, and the thick solid line shows the total absorption after convolution with the LSF, which fits the data. For the multi-component fits, the fits are constrained using information on the ISM velocity structure provided by previous analyses of Mg II and/or Fe II absorption lines.

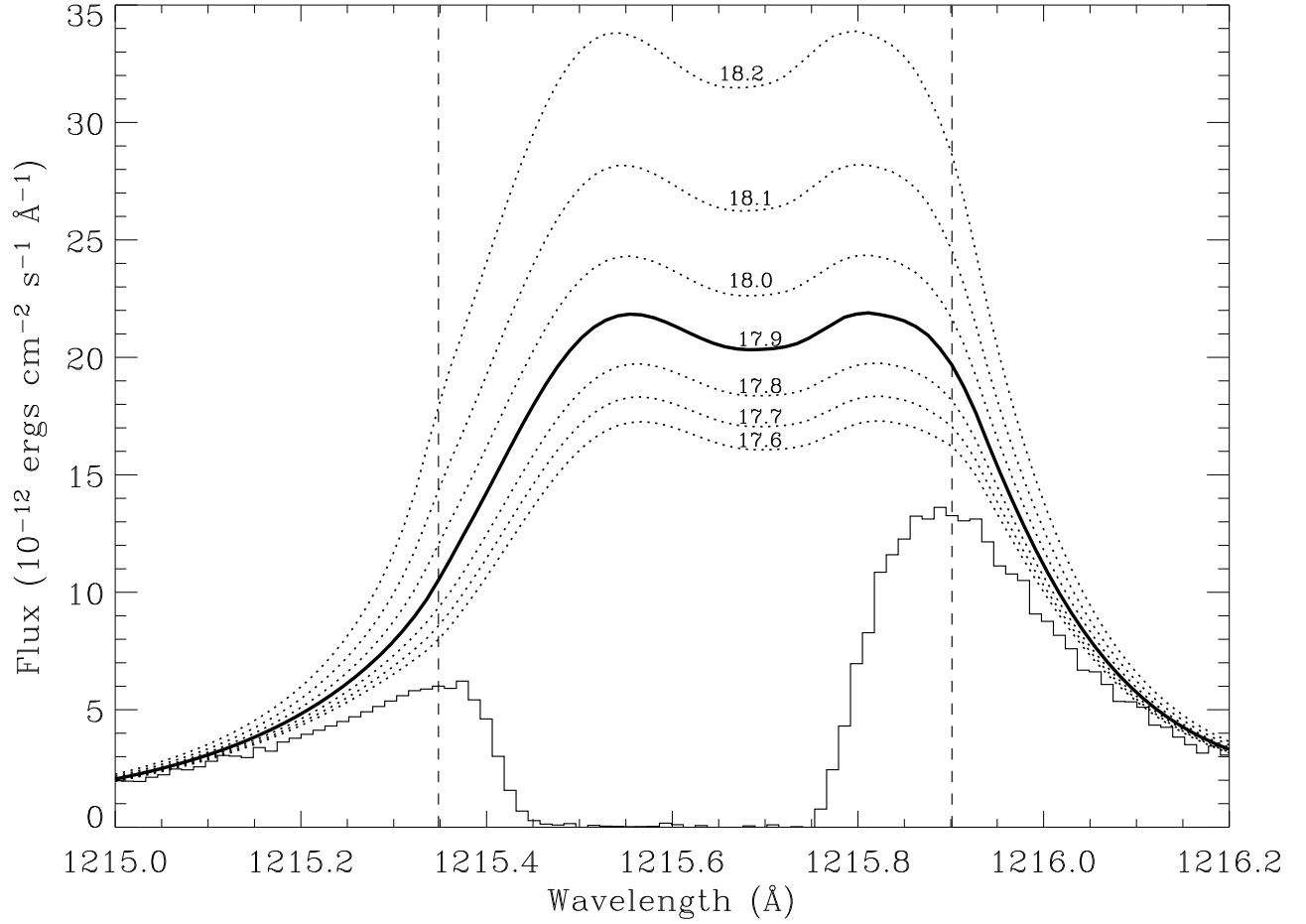


Fig. 4.— Reconstructions of the stellar Ly $\alpha$  emission line profile for  $\xi$  Boo A, assuming ISM H I column densities of  $\log N(\text{H I}) = 17.6 - 18.2$ . Outside of the dashed lines the profile is estimated by extrapolating upwards from the data based on the assumed  $\log N(\text{H I})$ , while inside of the dashed lines the profile shape is estimated from the observed profile of the Mg II h & k lines. Note that the D I absorption line at  $1215.25 \text{ \AA}$  has been removed. Measurements of the D I absorption suggest that the H I column density should be  $\log N(\text{H I}) = 17.9$ , assuming a canonical value of  $D/\text{H} = 1.5 \times 10^{-5}$ , so the profile constructed assuming this column density is emphasized in the figure.

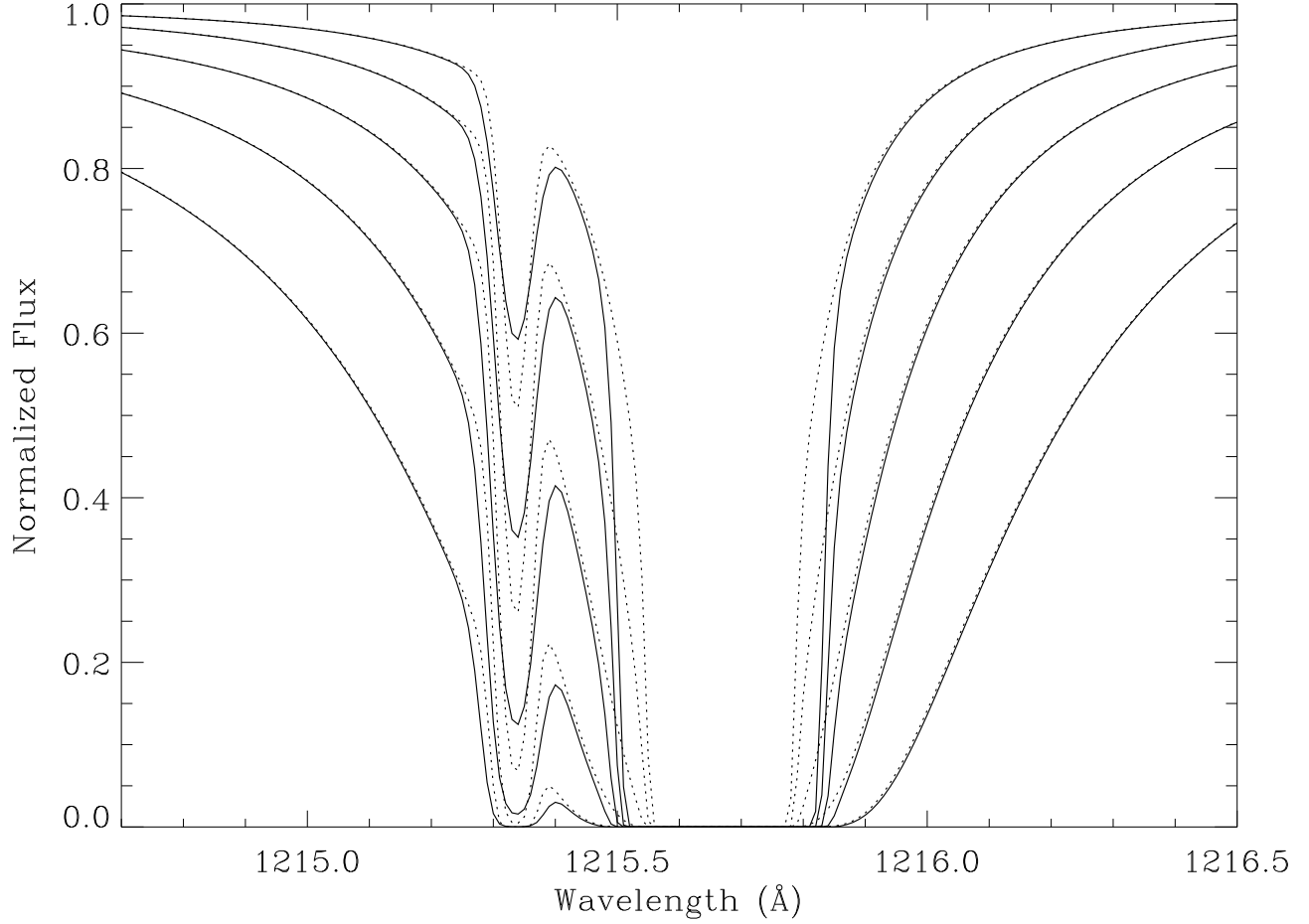


Fig. 5.— Absorption profiles for H I+D I Ly $\alpha$  absorption where the D I and H I parameters are related as described in the text, illustrating how absorption increases with increasing column density, where the profiles shown are for H I column densities of  $\log N(\text{H I}) = 17.5, 17.8, 18.1, 18.4,$  and  $18.7$ . The solid lines show the absorption for a Doppler parameter of  $b(\text{H I}) = 12.85 \text{ km s}^{-1}$  ( $T = 10,000 \text{ K}$ ), while the dotted lines show the absorption for  $b(\text{H I}) = 9.09 \text{ km s}^{-1}$  ( $T = 5000 \text{ K}$ ).

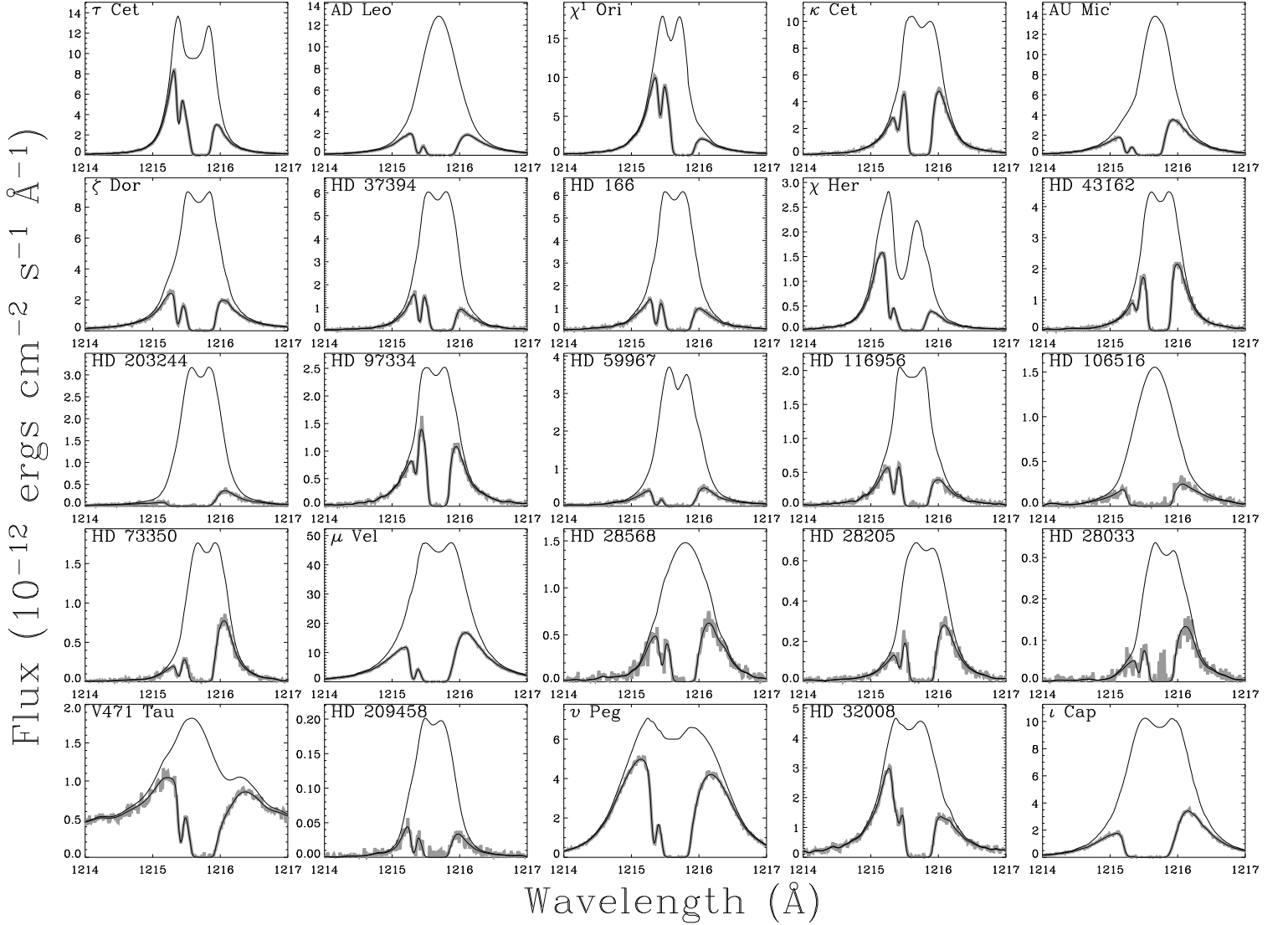


Fig. 6.— Our final best fits to the Ly $\alpha$  absorption spectra for the cases in which the ISM alone can account for all of the observed absorption. In each panel, the upper solid line is the reconstructed stellar line profile and the lower solid line is the fitted absorption profile, which fits the data (shaded line). The fit parameters are listed in Table 2, and integrated fluxes of the reconstructed stellar Ly $\alpha$  emission lines are listed in Table 3.

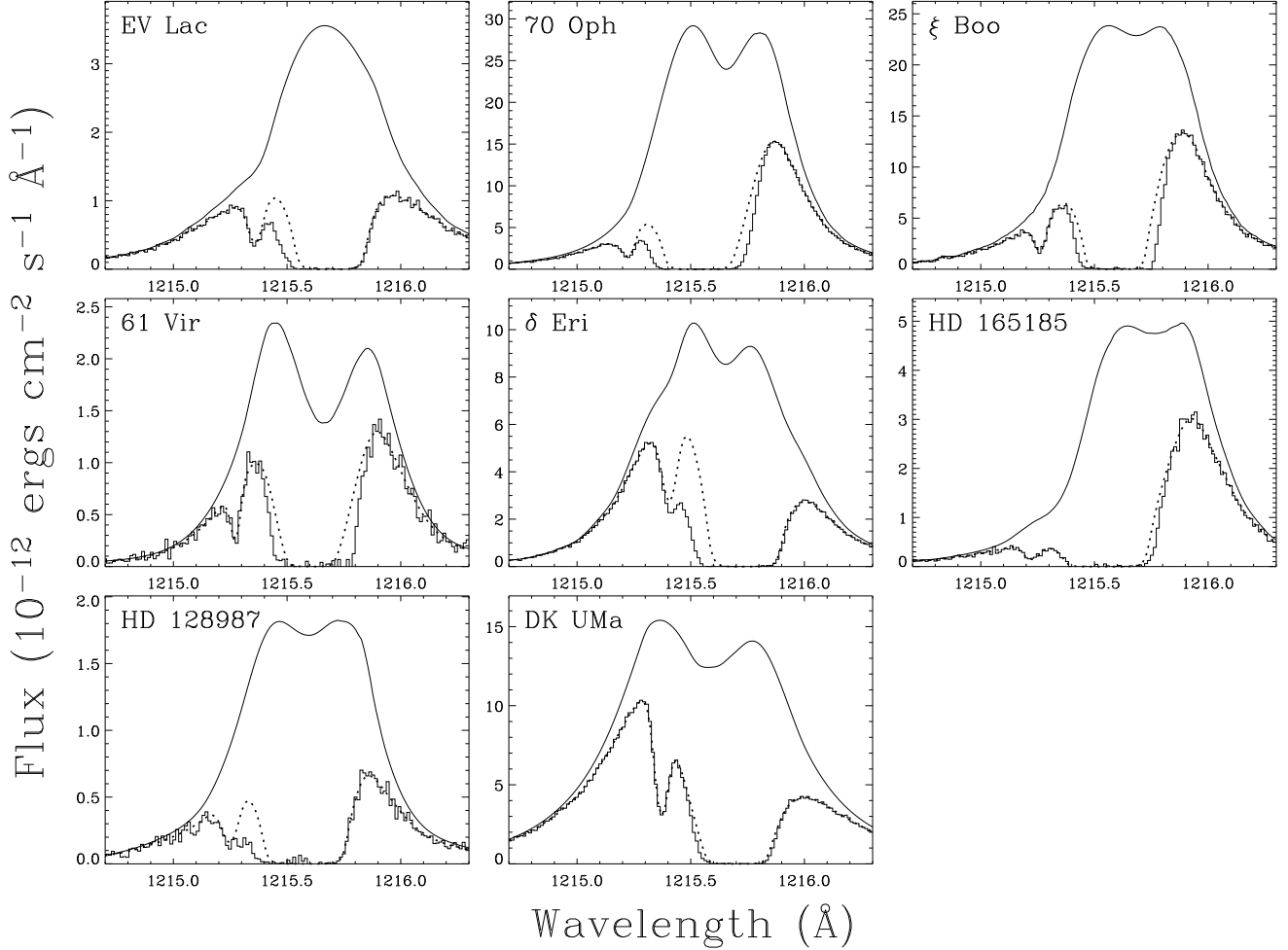


Fig. 7.— Our best fits to the Ly $\alpha$  absorption spectra for the cases in which HS/AS absorption components must be included in fits to the data, in addition to the ISM absorption. Rather than show the total absorption implied by the fit, we show the absorption only from the ISM absorption components (dotted lines), the discrepancy with the data indicating the excess absorption that must be accounted for by the HS/AS components. Excess absorption on the blue side of the line is interpreted as astrospheric absorption, and excess absorption on the red side of the line is assumed to be heliospheric. The fit parameters of these fits are listed in Table 2, and integrated fluxes of the reconstructed stellar Ly $\alpha$  emission lines are listed in Table 3.



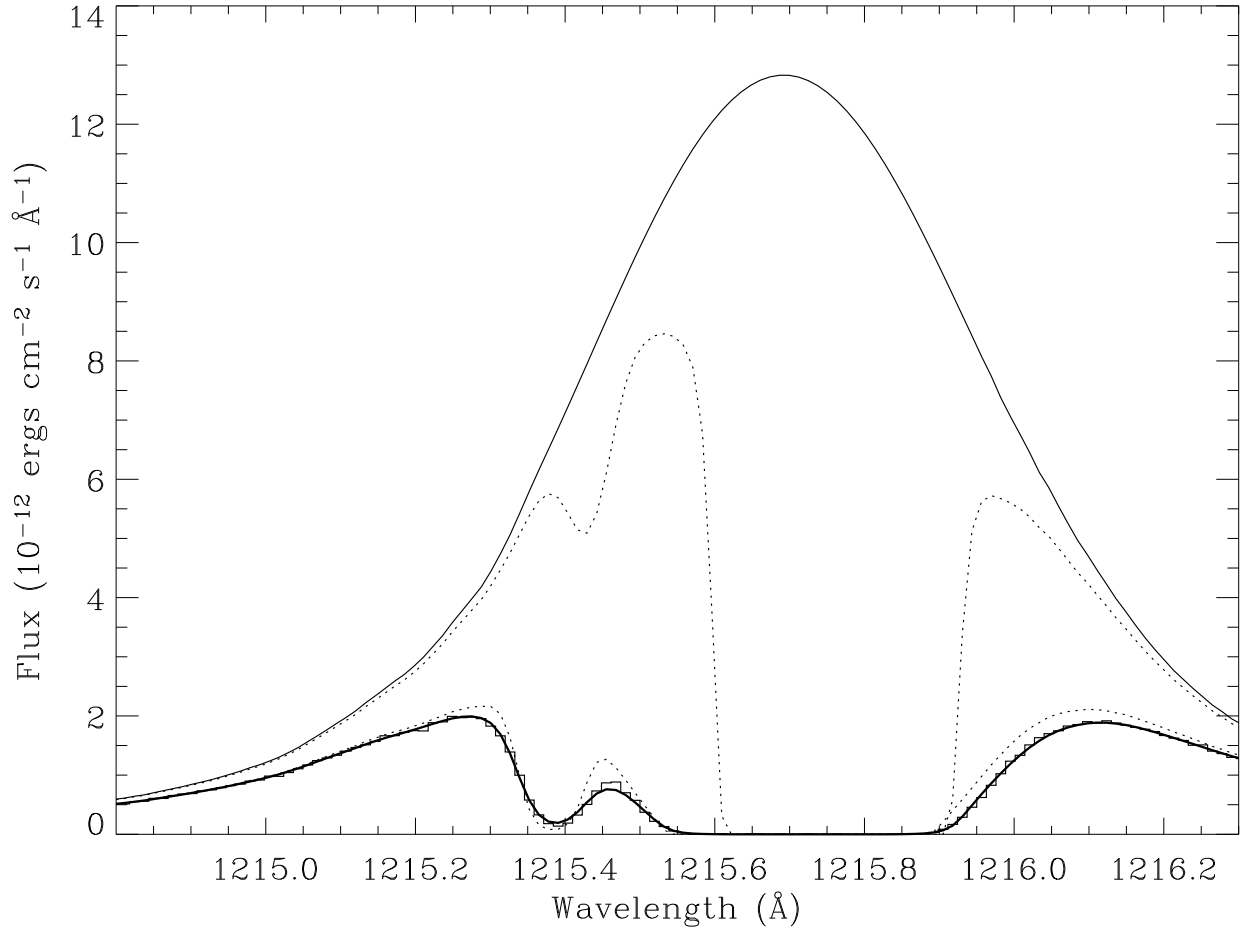


Fig. 8.— A two-component fit to the H I+D I Ly $\alpha$  absorption line seen towards AD Leo. The weaker component is assumed to be redshifted relative to the primary component by 12 km s $^{-1}$  and is forced to have a column density 10 times lower than the primary component. The Doppler parameters of the two components are forced to be equivalent, and in the fit they end up at  $b(\text{H I}) = 12.85$  km s $^{-1}$ . This is significantly lower than the value found for the single component fit in Fig. 7 (see Table 2), illustrating how multiple ISM components can artificially increase measured Doppler parameters when assuming a single component.

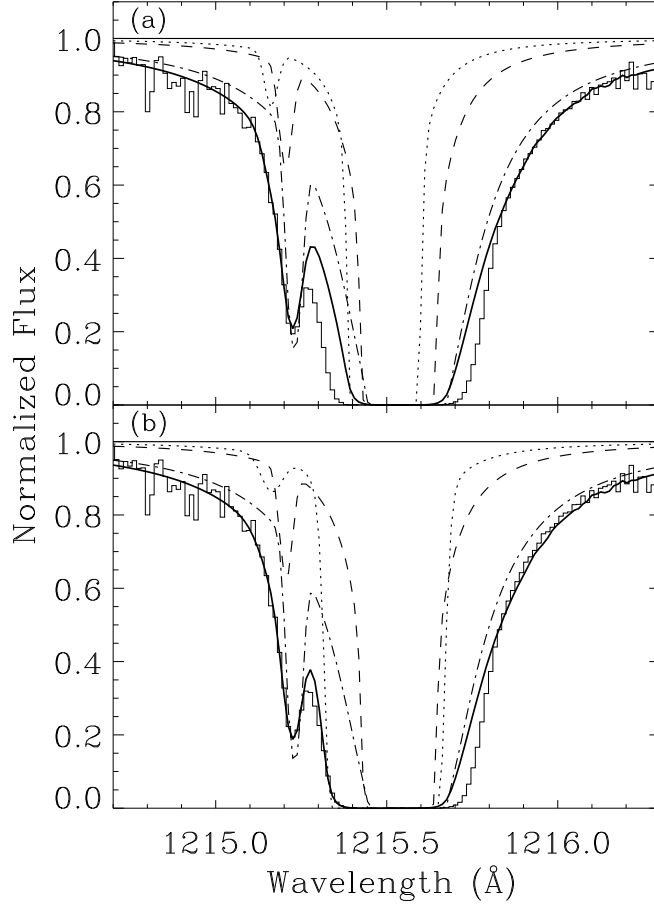


Fig. 9.— (a) A reproduction of the best 70 Oph fit from Fig. 7, but showing the individual ISM components as well as the total ISM absorption (thick solid line), where the dot-dashed, dashed, and dotted lines are absorption by ISM components 1, 2, and 3, respectively. The fit parameters are listed in Table 2. The excess absorption seen on the red and blue sides of the H I absorption is assumed to be heliospheric and astrospheric absorption, respectively. (b) A fit to the 70 Oph data like that in (a), but with component 3 (dotted line) allowed to have a Doppler parameter large enough to account for the excess absorption on the blue side of the H I absorption line. In this fit, the component 3 Doppler parameter is too large to be consistent with that measured for this component from Mg II absorption, so we conclude that this fit is unreasonable (see text).

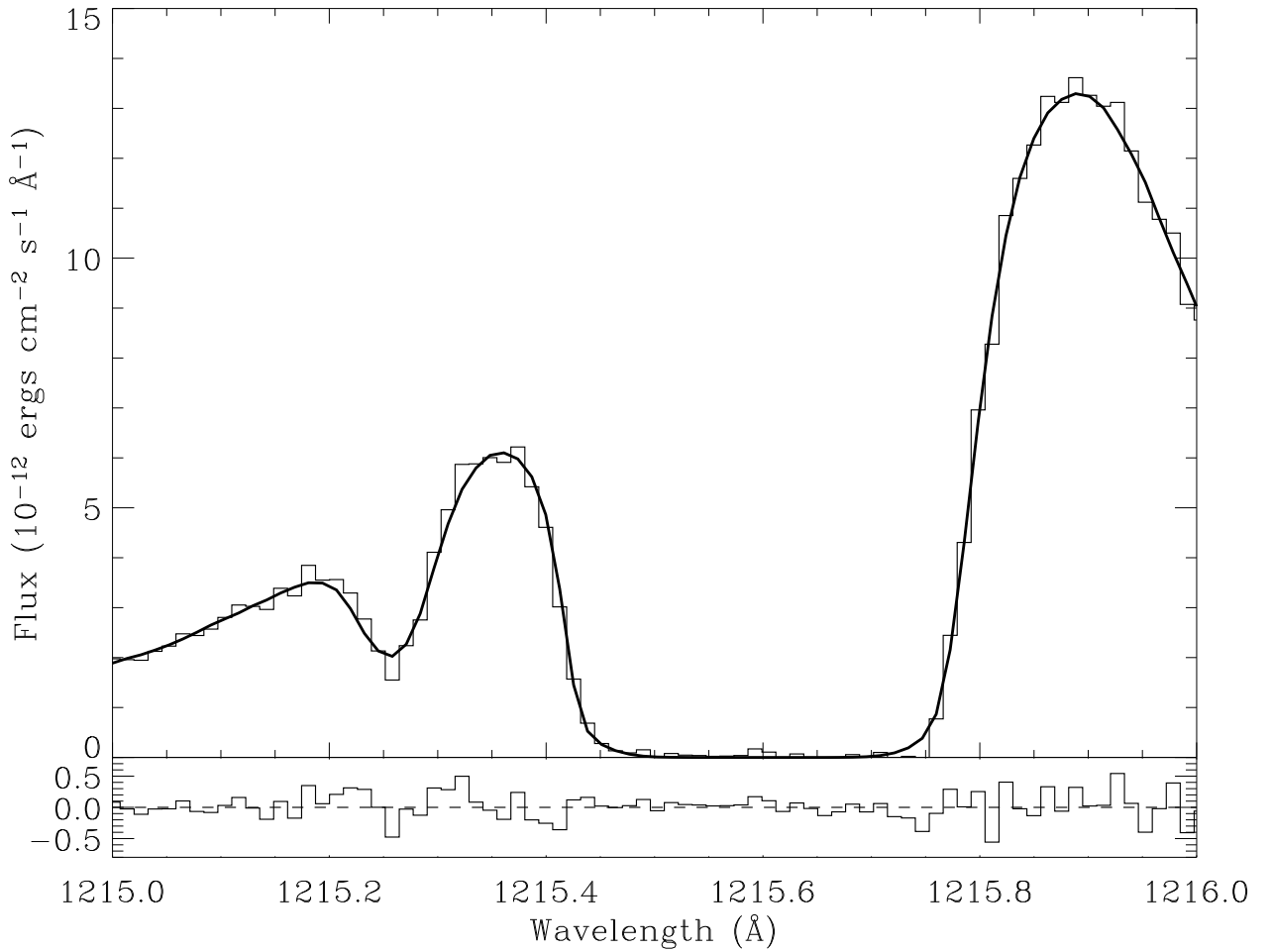


Fig. 10.— A fit to the Ly $\alpha$  absorption seen towards  $\xi$  Boo A, with residuals shown below the fit. The centroid of the HS/AS absorption is fixed such that it can only account for excess H I absorption on the red side of the line (i.e., heliospheric absorption) rather than the excesses on both sides of the line suggested by the fit in Fig. 7. This results in a poor fit to the D I absorption at 1215.25  $\text{\AA}$ . The D I fit is much too broad, demonstrating that the ISM H I and D I absorption must be narrower and the HS/AS component must therefore be allowed to contribute to the absorption on the blue side of the H I line as well as the red side. The implication is that astrospheric absorption is present towards  $\xi$  Boo.

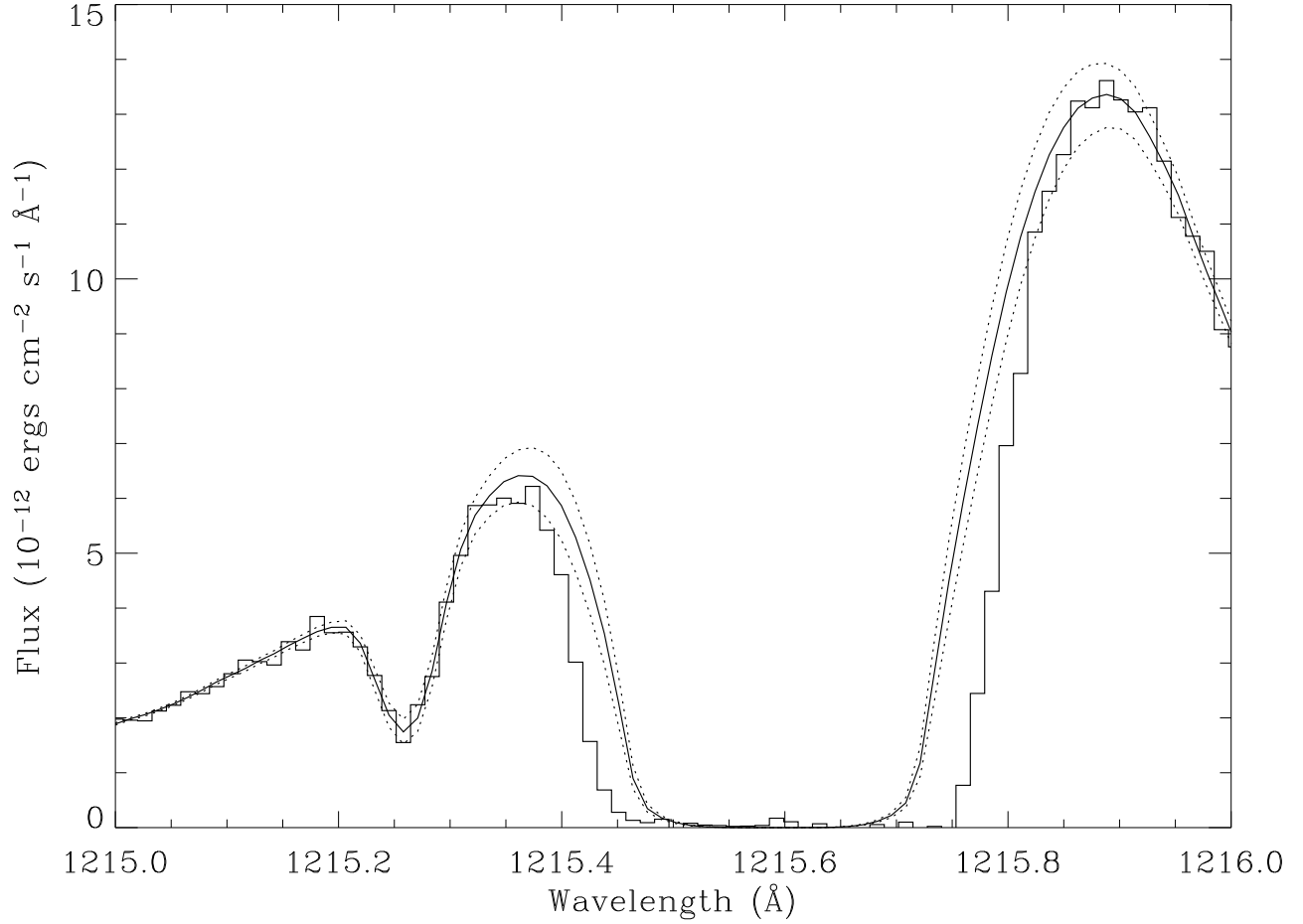


Fig. 11.— A reproduction of the best  $\xi$  Boo fit from Fig. 7 (solid line), but also showing the absorption profile that results when the H I column density is increased and decreased by 10% (dotted lines). A 10% increase in the column density clearly does not broaden the absorption enough to account for the excess H I absorption that we interpret as heliospheric and astrospheric absorption.

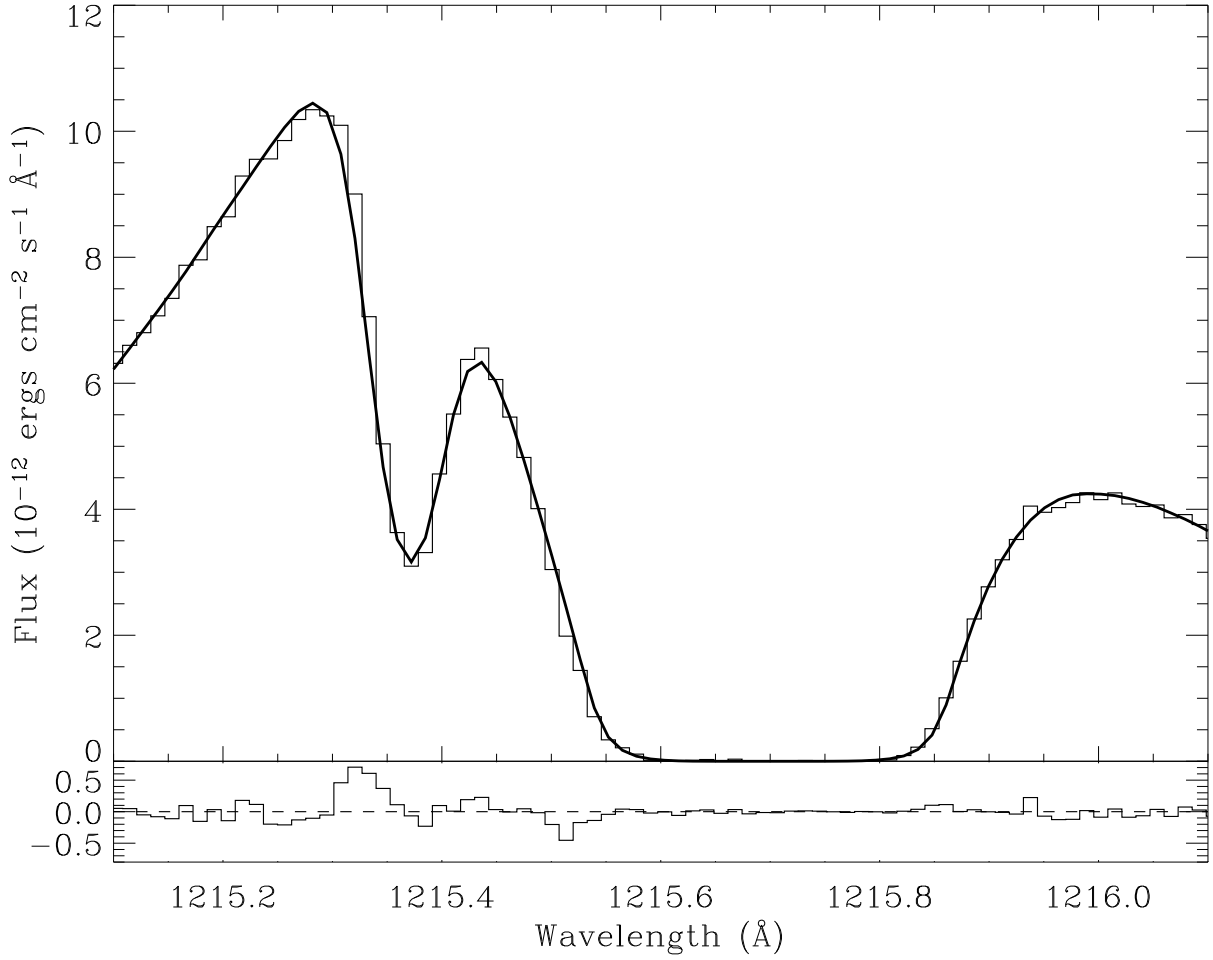


Fig. 12.— The best fit possible to the Ly $\alpha$  absorption observed towards DK UMa assuming that the absorption is entirely from the ISM, with residuals shown below the fit. The fit is poor along the blue sides of both the D I and H I lines near 1215.33  $\text{\AA}$  and 1215.51  $\text{\AA}$ , respectively. These discrepancies can be fixed by the addition of an HS/AS absorption component, as shown in Fig. 7. The discrepancies are somewhat subtle, but the S/N of the data is high enough for us to conclude that it is significant and indicative of at least a marginal detection of astrospheric absorption.

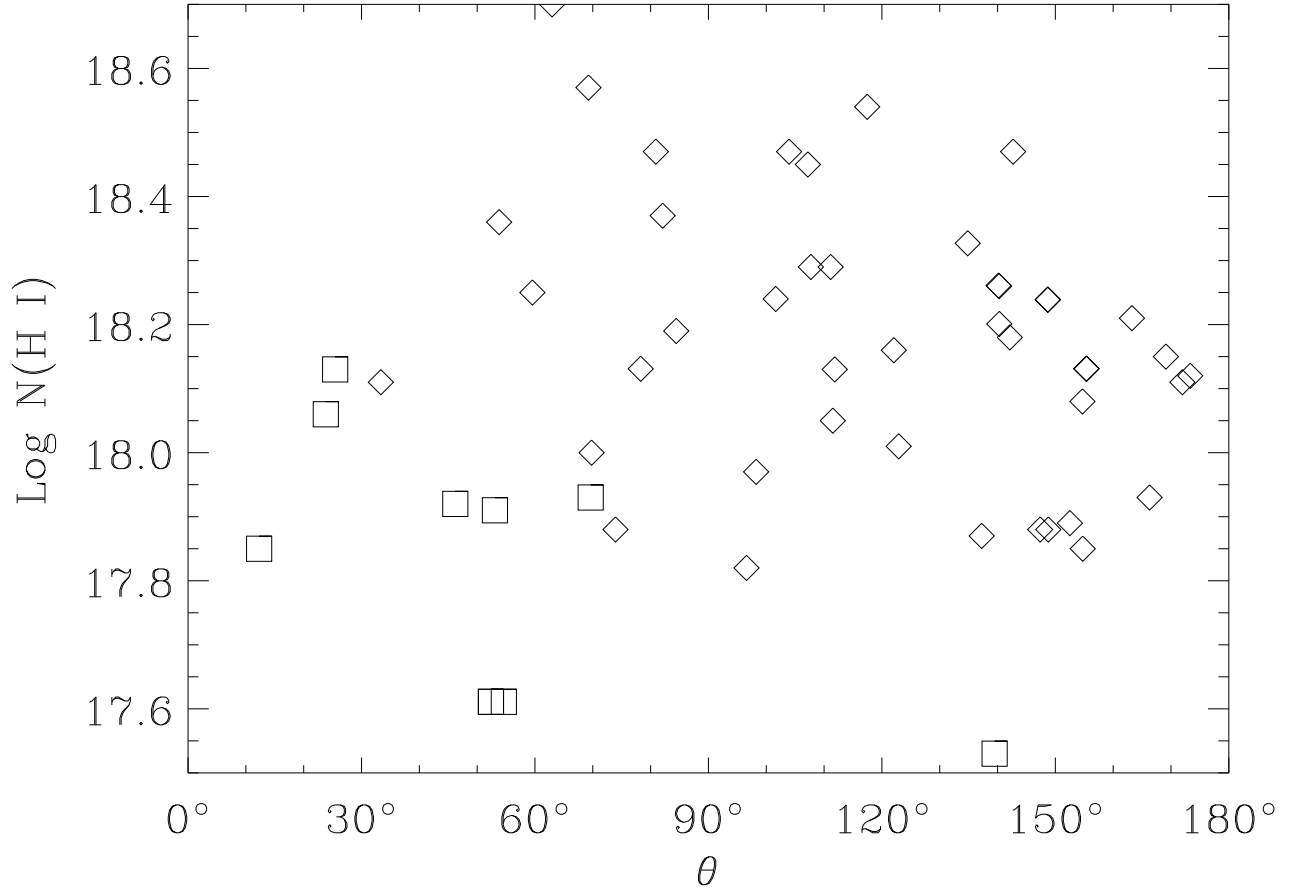


Fig. 13.— The ISM H I column densities measured for all HST-observed lines of sight are plotted versus the angle of the lines of sight relative to the upwind direction of the ISM flow seen by the Sun. The boxes and diamonds indicate lines of sight that yield detections and nondetections of heliospheric absorption, respectively.

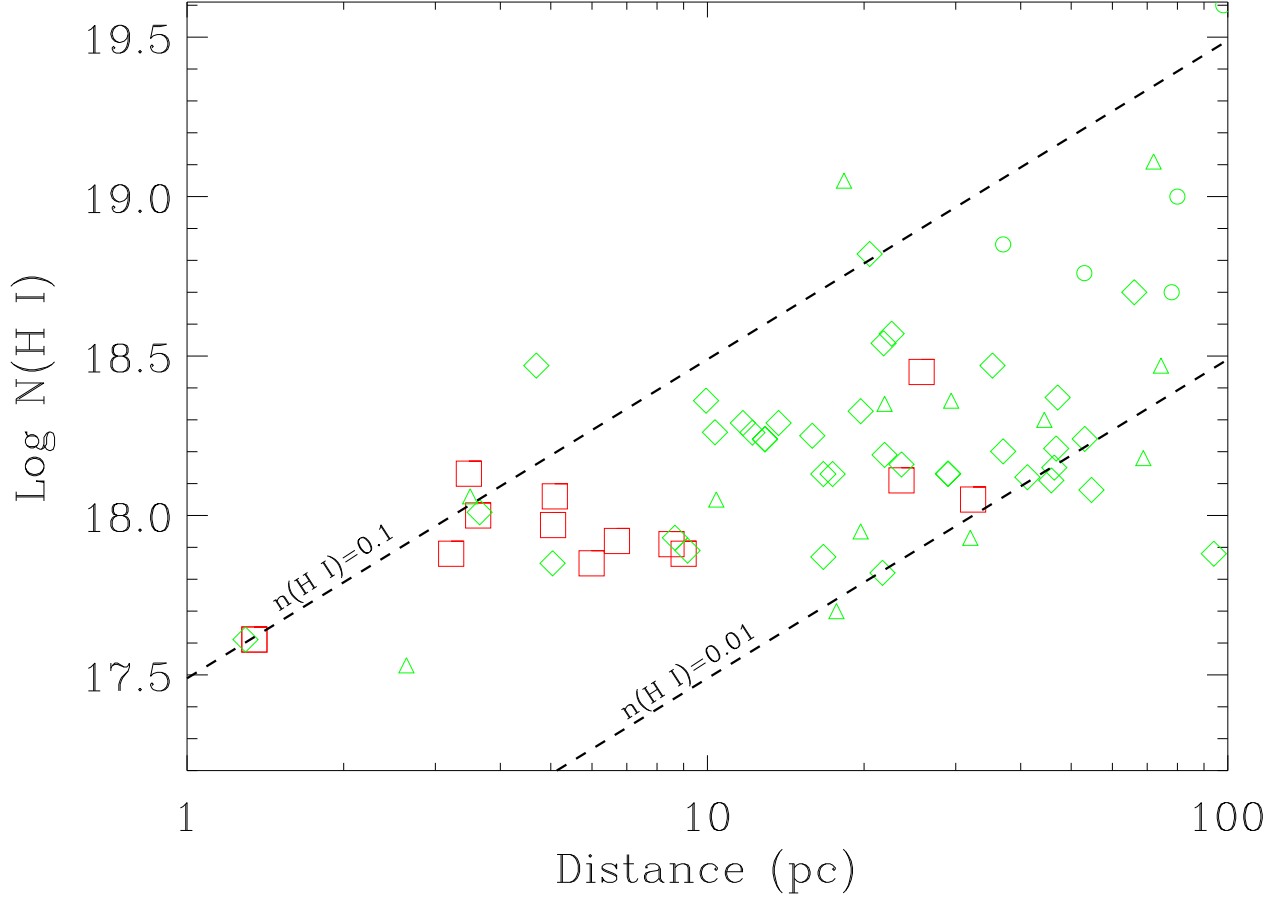


Fig. 14.— The ISM H I column densities measured for all HST-observed lines of sight are plotted versus distance. The red boxes are lines of sight that yield detections of astrospheric absorption, the diamonds are lines of sight that yield nondetections, and the triangles are lines of sight for which a valid search for astrospheric absorption is not possible (see text). Finally, the circles are a few additional measurements that are from EUVE or *Copernicus* instead of HST. The dashed lines are contours for line-of-sight average H I densities of  $n(\text{H I}) = 0.1 \text{ cm}^{-3}$  and  $n(\text{H I}) = 0.01 \text{ cm}^{-3}$ .

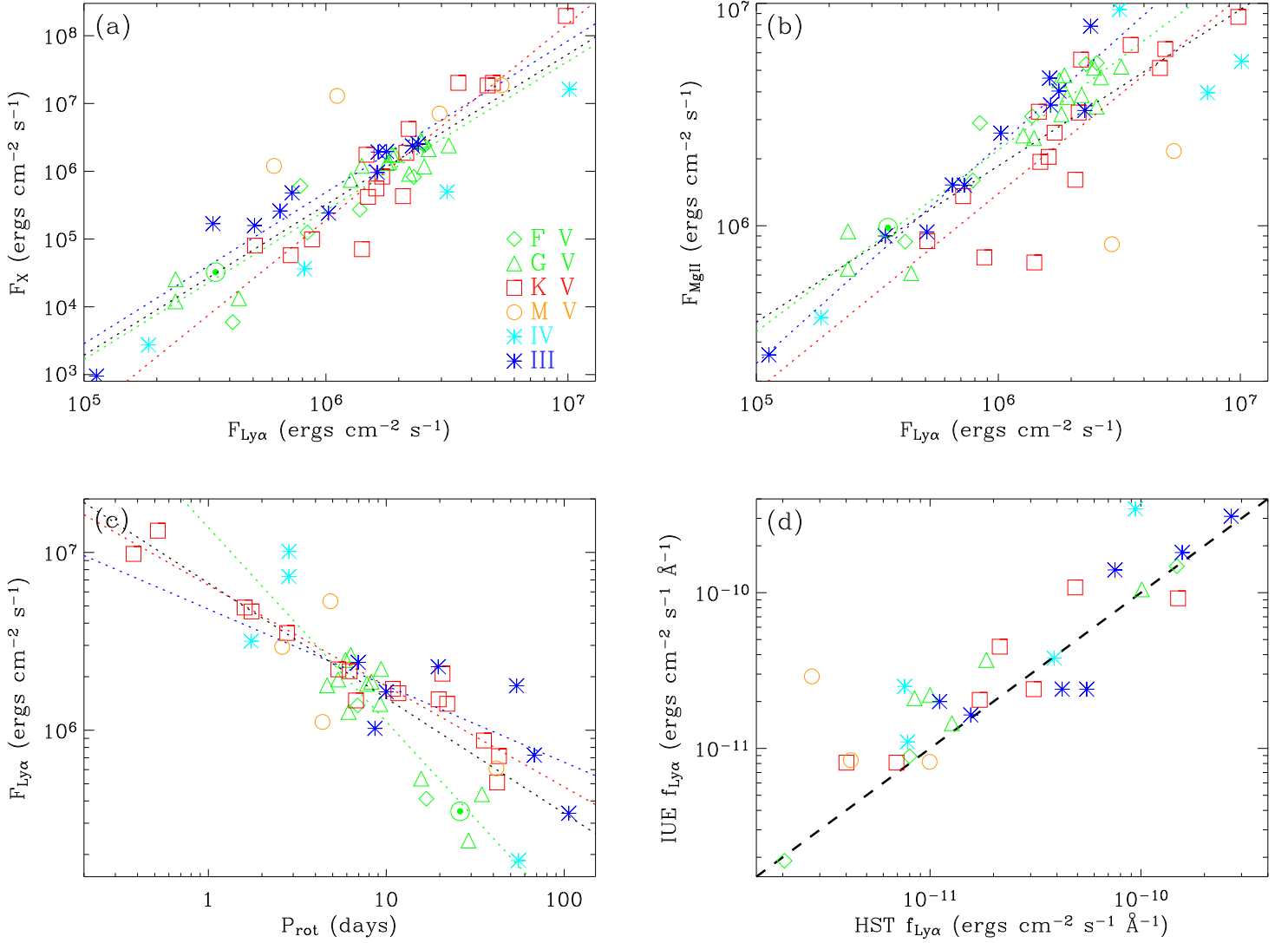


Fig. 15.— (a) X-ray surface flux plotted versus Ly $\alpha$  surface flux for the stars listed in Table 3, with the addition of a point representing the Sun ( $\odot$ ). Different symbols are used for different classes of stars. Dotted lines show various fits to the data, where the color of the line corresponds to the color of the data points being fitted. The black dotted line is a fit to all the data combined. (b) Mg II h & k surface flux plotted versus Ly $\alpha$  surface flux, where the lines and symbols are as in (a). (c) Ly $\alpha$  surface flux plotted versus rotation period, where the lines and symbols are as in (a). (d) Ly $\alpha$  fluxes measured by IUE from Landsman & Simon (1993) plotted versus the HST measurements, where the symbols are as in (a). The dashed line is the line of equivalency. Note that the parameters of the fits shown in (a)–(c) are listed in Table 4.